https://doi.org/10.5194/essd-2025-632
Preprint. Discussion started: 9 December 2025

Open Access Earth System Science Data Discussions

Mapping Three Decades of Urban Growth in China: A 30m Annual Building Height Dataset (1990 – 2019)

Yizhi Zhang[1], Yi Wang[1], Quanhua Dong[2,3], Xiao-Jian Chen[4], Fan Zhang[1], Xuecao Li[5], Yu Liu[1]

[1]Institute of Remote Sensing and Geographic Information System, Peking University, Beijing, 100871, China
[2]Key Laboratory of Radiometric Calibration and Validation for Environmental Satellites, National Satellite Meteorological Center (National Center for Space Weather), China Meteorological Administration, Beijing, 100081, China
[3]Innovation Center for FengYun Meteorological Satellite, Beijing, 100081, China
[4]School of Public Affairs, Xiamen University, Xiamen, 361005, China
[5]College of Land Science and Technology, China Agricultural University, Beijing, 100083, China

Correspondence to: Quanhua Dong (dqh@pku.edu.cn)

Abstract. Long-term building height data are critical for analyzing urban morphological evolution and renewal processes, yet such datasets at fine spatial resolutions remain scarce for large geographical regions. This study proposes a framework to generate continuous annual building height maps for China at 30 m spatial resolution from 1990 to 2019, integrating multi-source remote sensing data (Landsat, Sentinel-1/2, et. al) through the eXtreme Gradient Boosting (XGBoost) model. The framework reconstructs Vertical-Vertical (VV) band, incorporates reference data derived from the Continuous Change Detection and Classification (CCDC) algorithm, and utilizes Total Variation (TV) denoising to achieve temporal consistency, while retaining inter-annual building height variations. Validation results demonstrate stable performance of the building height estimates over the past three decades, with nationwide RMSE values ranging between 5.96 and 6.69 m. Comparisons with existing datasets confirm consistency with reference building heights and their temporal evolution driven by urban development and renewal. Furthermore, our dataset shows pronounced horizontal and vertical expansion of Chinese cities between 1990 and 2019, as the total impervious surface area increases from 56,413.68 to 174,320.66 km² and overall building volume rises from 471.24 to 884.69 km³. Provincial contributions to national building volume change substantially over time, with Hebei (12.9%), Shandong (11.4%), and Henan (10.3%) leading in 1990, while Shandong (10.0%), Guangdong (8.0%) and Jiangsu (8.0%) are in the leading positions in 2019. The resulting annual 30 m resolution building height datasets, made openly accessible, provide a valuable foundation for cross-city comparisons, long-term three-dimensional (3D) urban morphology studies, and policy-relevant planning in fast-growing Chinese cities.

1 Introduction

Building height, a fundamental metric of buildings, captures the vertical dimension of urban form as shaped by both human activity and the natural environment. Accurate mapping of building height enhances human settlement analyses and applications, such as 3D population distribution modeling (Alahmadi, Atkinson, and Martin, 2013), material stock quantification (Frantz et al., 2023), and well-being assessments (Schug et al., 2021). It also facilitates quantitative evaluation

https://doi.org/10.5194/essd-2025-632
Preprint. Discussion started: 9 December 2025

of interactions between buildings and natural environment, including urban heat island effects (Huang and Wang, 2019; Yang et al., 2021), pollution dispersion dynamics (Lyu et al., 2024), and energy consumption patterns (Resch et al., 2016). Moreover, temporal variations in building height reflect both construction and demolition activities, indicating vertical morphological transformations during urbanization (Cohen, 2015). Monitoring these changes is essential for understanding urban expansion and renewal, characterizing urban growth patterns, and guiding sustainable urban planning (Peters et al., 2022).

Optical and Synthetic Aperture Radar (SAR) satellite remote sensing data have become indispensable for large-scale building height mapping due to their seamless spatiotemporal coverage with mutli-dimensional land-surface information. Optical remote sensing data generally exploit shadows and morphological profiles to extract buildings of various heights (Qi et al., 2016). For instance, Geiß et al. (2020) applied ensemble regression to map building heights across four German cities using Sentinel-2 high-resolution optical imagery. Similarly, Sun et al. (2024) established a footprint-level Chinese building height dataset using Beijing-3 Very High Resolution (VHR) optical imagery combined with deep learning methods. SAR data serve as another important source for building height extraction, as microwave backscatters closely relate to building heights (Koppel et al., 2017). Li et al. (2020) utilized Sentinel-1 Vertical-Vertical (VV) and Vertical-Horizontal (VH) band data to produce an urban height dataset covering 96 U.S. cities. However, a single remote sensing data type often provides insufficient spectral or structural information, limiting the extraction accuracy of building heights. For example, optical data become unreliable in cloud-covered regions (Koppel et al., 2017), while SAR data tend to noised in areas with tall buildings (Yadav, Nascetti, and Ban, 2025).

Recent research increasingly integrates optical and SAR remote sensing data to generate building height products, harnessing their complementary strengths. For instance, Frantz et al. (2021) combined Sentinel-1 SAR with Sentinel-2 optical imagery to map building heights nationwide in Germany, while Yadav et al. (2025) generated a 10 m resolution map for four European countries using a deep learning model on Sentinel-1/2 time series data. Ancillary datasets, such as nighttime lights and population data, are also incorporated as covariates, improving building height estimation by capturing building characteristics and surrounding environmental contexts from multiple perspectives. Wu et al. (2023) produced China's first 10 m resolution national building height dataset by fusing Sentinel-1/2 imagery, nighttime light observations, and Digital Surface Model (DSM) data. Che et al. (2024) further advanced the field by integrating multi-source remote sensing data with architectural geometric features to produce the first global footprint-level building height dataset with an XGBoost model. Despite these advances, most existing datasets remain static, mapping building heights for only a single year due to limited reliable reference data. In addition, the restricted temporal span of high-resolution satellite systems such as Sentinel-1/2 hampers detailed historical mapping, particularly before 2010.

Constructing long-term building height datasets requires multi-temporal remote sensing observations. Frolking et al. (2022) developed a global microwave backscatter coefficient dataset from multiple scatterometers spanning 1993-2020, yet its 0.05° spatial resolution (roughly equivalent to 5 km at the equator) limits its applicability for microscale urban analysis. Higher-resolution, long-term building height mapping has been pursued through machine and deep learning methods that integrate multi-source, multi-decadal datasets. Using a morphology-based method, He et al. (2023) produced a China's 30 m resolution

https://doi.org/10.5194/essd-2025-632
Preprint. Discussion started: 9 December 2025

building height dataset from 1990 to 2010 by fusing Advanced Land Observing Satellite (ALOS) DSM with the Landsat-derived Global Artificial Impervious Area (GAIA) data. Yan et al. (2024) trained a random forest model on 2019 building height reference data, Landsat optical imagery, and socioeconomic variables, directly applying it to other years and thereby generating 1 km resolution height estimates for 2001-2019 across China. Nevertheless, these datasets largely neglect not only urban renewal but also complicated urban built and demonish process. They are unreliable for regions undergoing frequent demolition–reconstruction cycles, where historical height records often deviate substantially from present conditions.

To account for urban renewal processes, Wang et al. (2023) proposed a temporal segmentation algorithm applied to Landsat time series, identifying urban renewal zones in Beijing and interpolating heights from 1990 to 2020 using logistic reasoning. However, this approach relied on manually selected thresholds, limiting its extrapolation to other regions. Chen et al. (2025) addressed these limitations by generating reliable height reference data across multiple years and fully exploiting long-term Landsat observations. They integrated spaceborne LiDAR data from the Global Ecosystem Dynamics Investigation (GEDI) as height benchmarks. Reference height data were then extracted for specified years using the Continuous Change Detection and Classification (CCDC) algorithm to detect land use change, and a deep learning method was applied to Landsat archives to map built-up heights. This framework produced 30 m resolution building height datasets for China in 2005, 2010, 2015, and 2020. Nevertheless, it depends on Phased Array L-band Synthetic Aperture Radar (PALSAR) data, which cover only limited years (2007, 2009–2010, 2015, 2019–2020), making height mapping for the intervening years a challenging task.

Continuous annual building height datasets are crucial for detecting building demolition and reconstruction at fine spatio-temporal scales during urban growth and renewal. However, existing long-term building height datasets either lack scalability to broader spatial extents or fail to capture year-to-year changes. To address this gap, this study aims to generate annual building height maps for China from 1990 to 2019 at 30 m resolution. First, we establish a framework based on the eXtreme Gradient Boosting (XGBoost) model that integrates multi-source, multi-temporal, and multi-decadal remote sensing data (including optical, SAR, and terrain information) for long-term building height estimation. The VV band is reconstructed from 1990 to 2014 to enhance estimation accuracy, providing continuous signals that reflect latent building-height features. Second, to account for urban renewal, the CCDC algorithm is applied to generate annual reference height data through land-use transition detection, and the Total Variation (TV) denoising is utilized to improve the stability and reliability of building height time series. Finally, the accuracy of multi-year building height estimates is evaluated through comparisons with existing datasets and historical remote sensing imagery, while the mapped spatio-temporal dynamics of building height and volume provide additional evidence of the dataset's ability to accurately represent urban growth and renewal.

2 Datasets

Remote sensing data we used is from multiple public access Earth observation sources, including optical data, radar data, terrain data and products derived from remote sensing images. All data preprocessing procedures are conducted on the Google Earth Engine (GEE) platform (Gorelick et al., 2017). Google Earth Engine is a cloud platform hosting public satellite imagery

https://doi.org/10.5194/essd-2025-632
Preprint. Discussion started: 9 December 2025

and derived products (e.g. Landsat, Sentinel, SRTM) with scalable server-side processing. Data acquired from and preprocessed on GEE are detailed in Table 1.

Table 1. Data utilized to map long-term building heights

Data	Parameters	Original Resolution	Time Period	Source
Landsat 5	Blue; Green; Red; NIR; SWIR1; SWIR2	30 m	1990-2011	"LANDSAT/LT05/C02/T1_L2" (Earth Engine Snippet)
Landsat 7	Blue; Green; Red; NIR; SWIR1; SWIR2	30 m	2000-2019	"LANDSAT/LE07/C02/T1_L2" (Earth Engine Snippet)
Landsat 8	Blue; Green; Red; NIR; SWIR1; SWIR2	30 m	2014-2019	"LANDSAT/LC08/C02/T1_L2" (Earth Engine Snippet)
Sentinel-1	VV; VH	10 m	2015-2019	"COPERNICUS/S1_GRD" (Earth Engine Snippet)
Sentinel-2	Aerosols; Water vapor; Red Edge 1-4	10 m	2018-2019	"COPERNICUS/S2_SR_HARMONIZED" (Earth Engine Snippet)
Shuttle Radar Topography Mission (SRTM)	Elevation; Slope	30 m	2000	"USGS/SRTMGL1_003" (Earth Engine Snippet)
ALOS World 3D - 30m (AW3D 30)	DSM	30 m	2010	"JAXA/ALOS/AW3D30/V4_1" (Earth Engine Snippet)
Location	Latitude; Longitude	/	2019	"ESA/WorldCover/v100" (Earth Engine Snippet)

https://doi.org/10.5194/essd-2025-632
Preprint. Discussion started: 9 December 2025

Open Access Earth System Science Data Discussions

GAIA	Settlement Coverage	30 m	1990-2018	"Tsinghua/FROM-GLC/GAIA/v10" (Earth Engine Snippet)
World Settlement Footprint (WSF) 2019	Settlement Coverage	10 m	2019	"projects/sat-io/open-datasets/WSF/WSF_2019" (Earth Engine Snippet)
Google CCDC	tBreak	30 m	1999-2019	"GOOGLE/GLOBAL_CCDC/V1" (Earth Engine Snippet)
The 2019 Reference Data	Building Height	Vector	2019	https://map.baidu.com/

2.1 Landsat images

Landsat surface reflectance time series data from 1990 to 2019 is utilized. It has been atmospheric corrected through the Landsat Ecosystem Disturbance Adaptive Processing System (LEDAPS) (Masek et al., 2006) and Land Surface Reflectance Code (LaSRC) (Vermote et al., 2016). The spectral bands include Blue, Green, Red, Near Infrared (NIR), Shortwave Infrared 1 (SWIR1), and Shortwave Infrared 2 (SWIR2). Five more indices are further derived: the Normalized Difference Vegetation Index (NDVI), as defined in Eq. (1); the Enhanced Vegetation Index (EVI), given by Eq. (2); the Land Surface Water Index (LSWI) from Eq. (3); the Modified Normalized Difference Water Index (MNDWI) according to Eq. (4), and Normalized Difference Built-up Index (NDBI) in Eq. (5). These indices' predictive validity have been demonstrated in previous researches (Wu et al., 2023; Li et al., 2020):

$$NDVI = \frac{\rho_{NIR}-\rho_{red}}{\rho_{NIR}+\rho_{red}}, \quad (1)$$

$$EVI = \frac{2.5(\rho_{NIR}-\rho_{red})}{(\rho_{NIR}+6\rho_{red}-7.5\rho_{blue}+1)}, \quad (2)$$

$$LSWI = \frac{\rho_{NIR}-\rho_{SWIR\,1}}{\rho_{NIR}+\rho_{SWIR\,1}}, \quad (3)$$

$$MNDWI = \frac{\rho_{green}-\rho_{SWIR\,1}}{\rho_{green}+\rho_{SWIR\,1}}, \quad (4)$$

$$NDBI = \frac{\rho_{SWIR\,1}-\rho_{NIR}}{\rho_{SWIR\,1}+\rho_{NIR}}, \quad (5)$$

https://doi.org/10.5194/essd-2025-632
Preprint. Discussion started: 9 December 2025

where ρ_{NIR}, ρ_{red}, ρ_{blue}, $\rho_{SWIR\ 1}$ and ρ_{green} each equals the pixel value of the corresponding band in Landsat. Images from Landsat 5 Thematic Mapper (TM), Landsat 7 Enhanced Thematic Mapper Plus (ETM+), and Landsat 8 Operational Land Imager/Thermal Infrared Sensor (OLI/TIRS) are concatenated to form a long-term dataset. Cloud-covered pixels are masked using the QA_PIXEL band. For each year's available imagery, three statistical composites are computed per pixel: median reflectance values representing central tendency, maximum values capturing spectral extremes, and standard deviation quantifying temporal variability (Wu et al., 2023).

2.2 Sentinel-1 and Sentinel-2 data

VV and VH backscatters in Sentinel-1 SAR data are selected for building height prediction during 2015-2019, with the VV backscatter subsequently serving as reference data later for 1km VV backscatter reconstruction. For Sentinel-2 multispectral imagery, six distinctive bands absent in Landsat sensors are utilized to enhance height estimation accuracy for the 2018-2019 period: Red Edge 1-4, Aerosol and Water Vapor. Cloud masking is implemented using the QA60 quality assessment band, followed by median value compositing to generate annual cloud-free Sentinel-2 reflectance products.

2.3 Terrain data

The ALOS World 3D-30m (AW3D30) DSM and the Shuttle Radar Topography Mission Digital Elevation Model (SRTM DEM) are integrated. While the SRTM DEM serves as the primary topographic predictor for building height regression, the AW3D30 DSM contributes to 1km VV backscatter reconstruction. Although DSMs like AW3D30 are widely adopted in single-year height estimations (Huang et al., 2022), their constrained temporal coverage (2006-2011) introduces chronological inconsistencies in long-term estimations. DEM data is deliberately selected since it predominantly captures terrain geometry rather than structures above surface. Furthermore, longitude and latitude are incorporated as additional predictors to account for spatial heterogeneity effects across China's vast territory (Yan et al., 2024).

2.4 Human settlement footprint

Two global human settlement footprint products are used: GAIA (Gong et al., 2020) and WSF (Marconcini et al., 2021). World Settlement Footprint (WSF) dataset, initially at 10m spatial resolution, is resampled to 30m to match our analytical grid. These datasets are applied to keep our research area within human settlement, with GAIA used for 1990-2018 and WSF 2019 for 2019.

2.5 Google global Landsat-based CCDC segments

The CCDC algorithm has been widely adopted for identifying temporal patterns of land-use transitions (Hu et al., 2024; Stanimirova et al., 2023). The Google CCDC dataset is generated by applying the algorithm proposed by Zhu and Woodcock (2014) to the complete Landsat image archive from 1999 to 2019, generating multi-layered outputs that include temporal

https://doi.org/10.5194/essd-2025-632
Preprint. Discussion started: 9 December 2025

breakpoint detection, observation counts, and breakpoint confidence levels. The original algorithm achieves a producer's accuracy of 97.72%, user's accuracy of 85.60%, and overall accuracy of 91.80%, demonstrating its reliability. The CCDC change detection results is employed as a temporal filter to exclude recently renewed urban areas from reference data.

2.6 The 2019 reference data

The 2019 reference data for building heights are derived from building footprint records of that year from Baidu Maps, covering 59 Chinese cities (Fig. 1). As the original data provide only building floor counts, they are converted into height estimates by multiplying by 3 meters per floor, a widely adopted method (Wu et al., 2023). This dataset has been validated by Liu et al. (2021), reporting 86.8% vertical accuracy with a mean height deviation of approximately 1 meter.

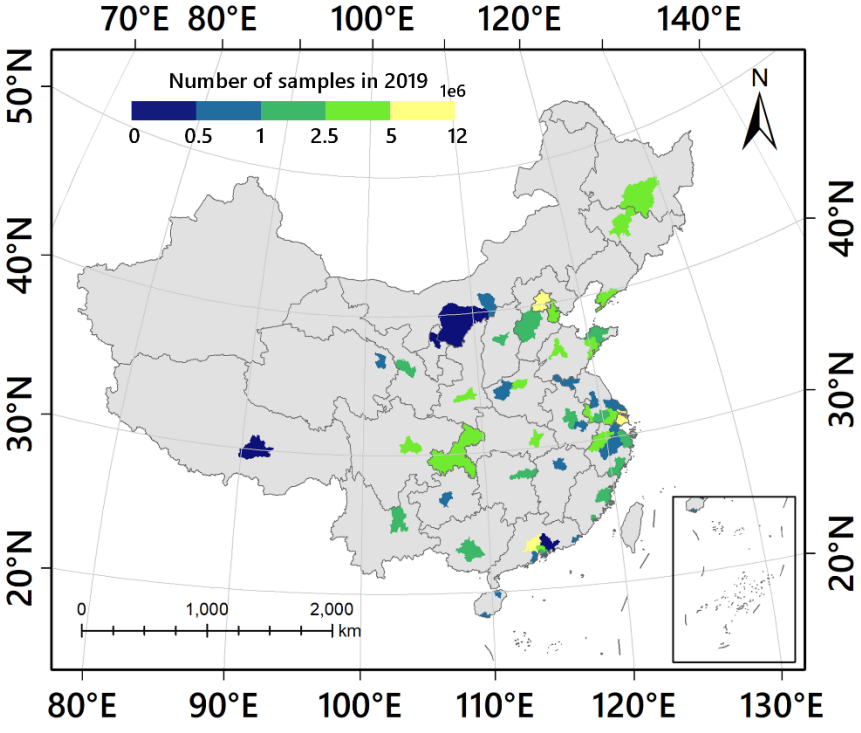

Figure 1: Number of sample pixels in 2019 in every sampled city.

To generate rasterized reference data for 2019, vector footprints are converted to 1m resolution height raster to preserve height details. Then, these raster datasets are resampled to 30m, averaging the value of every 1m pixel within the 30mx30m area (Zhou et al., 2022). Assuming the building height on a 1m pixel i within a 30m pixel is H_i^{1m}, then the resampled height H^{30m} is calculated in Eq. (6):

$$H^{30m} = \frac{\sum_i^{900} H_i^{1m}}{900}, \quad (6)$$

https://doi.org/10.5194/essd-2025-632
Preprint. Discussion started: 9 December 2025

Open Access Earth System Science Data Discussions

3 Method and validation

The proposed method consists of four main steps (Fig.2): First, to obtain reference building heights for years prior to 2019, the study area is delineated using GAIA and WSF 2019 settlement datasets, and reference samples for each year are extracted by Google CCDC Segments. To address the limited temporal coverage of SAR data, long-term VV backscatter at 1km spatial resolution for 1990-2014 is consturcted by Random Forest model based on Landsat spectral indices and SRTM DEM (Fig.2a). Second, XGBoost-based height regression models are trained for each year from 1990 to 2019 according to the annual reference data, and TV denoising is applied to post-process (Fig.2b). Third, the accuracy of the models is evaluated and compared (Fig.2c), and the patterns of urban growth and renewal are analyzed (Fig.2d).

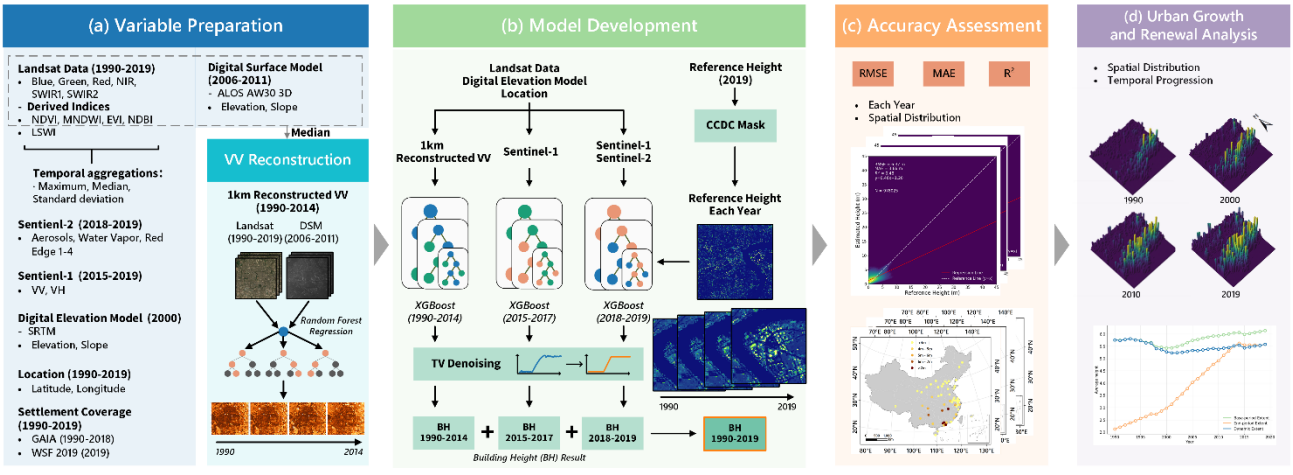

Figure 2: The framework for annual building height mapping. (a) Variable preparation; (b) Model development; (c) Accuracy assessment; (d) Urban growth and renewal analysis.

3.1 Variable preparation

3.1.1 Annual reference building heights from 1999 to 2019

This study employs three basic types of land-use conversion scenarios established in previous literature (Huang, Cao and Li, 2020; Stilla and Xu, 2023; Zhao, Xia and Li, 2023), to generate annual reference building height that account for urban renewal. The scenarios are defined as follows:

(1) New construction: areas transition from non-building land cover (e.g., water, grassland, barren land) to built-up/impervious land, characterized by the emergence of new buildings and an increase in height from zero.

(2) Complete demolition: areas transition from building to non-building, defined by the removal of structures, resulting in a decrease in height to zero.

(3) Persistent built-up: areas with no land-use conversion, where building heights generally remain stable. Minor

https://doi.org/10.5194/essd-2025-632
Preprint. Discussion started: 9 December 2025

variations may occur due to the reconstruction of existing structures.

Urban renewal is represented by the combined effect of these conversion types, capturing distinct trajectories of building height change.

New construction areas are identified using the GAIA and WSF 2019 settlement datasets. Complete demolition areas are inherently absent from the 2019 reference data. However, GAIA and WSF 2019 cannot capture demolition process, as they only identify new impervious surfaces and neglect conversions from building to non-building. To address this limitation, the CCDC is applied to identify persistent built-up areas based on the 2019 reference data. These areas are then used to derive annual reference building heights.

The CCDC mask records time of the last detected breakpoint. For a given year, only pixels with no breakpoint within the time period between this year and 2019 are kept as the reference data for this year. The absence of a breakpoint implies a high probability that these pixels experience no land-use transitions, therefore buildings within are neither newly constructed nor demolished, and thus retain the building height from the 2019 reference data. Although CCDC data cover the period from 1999 to 2019, China's urbanization before 1999 was predominantly new district development rather than systematic urban renewal (Wu, 2016). Consequently, the 1999 CCDC masks are uniformly applied to 1990-1999, which introduce negligible effects on reference data accuracy. Chen et al. (2025) adapted a similar approach of extracting long-term building height labels using CCDC dataset, with labels derived from 2020 to 2005, 2010 and 2015 achieving accuracy of over 85%, granting the reliability of applying CCDC to obtain annual reference data.

3.1.2 Reconstruction of VV band

Radar backscatters are widely utilized to develop building height datasets since they often bear valuable height information (Li et al., 2020; Yadav, Nascetti and Ban, 2025; Wu et al., 2023; Frantz et al., 2021). However, the access of long-term high-resolution open-source radar data is of great limitation due to security reasons. Sentinel-1 as the main source of radar present only covers the time period since 2014-10-03.

To acquire a long-term radar data, the Random Forest regression framework is adapted to fit 1km-resolution Sentinel-1 VV backscatter with Landsat spectral bands and terrain information (Yuan et al., 2024). It achieved satisfactory performance (RMSE = 1.5 dB) in the Beijing-Tianjin-Hebei region. The regression framework is further extended nationwide in this study, and the regressed VV backscatter is utilized as an independent variable for subsequent 30m-scale modeling. The predictor matrix includes six primary spectral bands (Blue, Green, Red, NIR, SWIR1, SWIR2), four indices (NDVI, EVI, MNDWI, NDBI), DEM, and DEM-derived slope. The reconstruction process is illustrated in Supplementary Fig. S4.

3.2 Model training

XGBoost models are adopted due to their demonstrated computational efficiency and predictive accuracy in prior architectural height regression studies (Che et al., 2024; Stipek et al., 2024). For each year, an independent XGBoost model is trained with

https://doi.org/10.5194/essd-2025-632
Preprint. Discussion started: 9 December 2025

year-specific variables extracted from remote sensing data, paired with corresponding reference building heights derived from CCDC masks. This approach maximizes the utility of annual data characteristics in the estimation process.

Given the limited temporal coverage of observation data, the set of predictor variables varies accorss years. Accordingly, three model configurations are constructed (Table 2). XGB-ReVV is applied from 1990 to 2014, using 15 predictors including Landsat spectral bands, reconstructed VV, elevation, slope, and location. XGB-S1 is employed for 2015–2017, replacing reconstructed VV with Sentinel-1 VV and VH backscatter. XGB-S1S2 is used for 2018–2019, further incorporating Sentinel-2 spectral bands in addition to the variables used in XGB-S1.

Hyperparameter optimization is conducted using Ray Tune exclusively on the 2019 dataset, and the optimized parameters are subsequently fixed to all earlier years.

Table 2. Independent variables used for different time periods

Model	Estimated Years	Independent Variables for each year	The numbers of variables
XGB-ReVV	1990-2014	Landsat 5-7-8 median, maximum, standard deviation (blue, red, green, NIR, SWIR1, SWIR2, NDVI, EVI, MNDWI, NDBI, LSWI), Regressed 1km VV, Elevation, Slope, Location	38
XGB-S1	2015-2017	Landsat 7-8 median, maximum, standard deviation (blue, red, green, NIR, SWIR1, SWIR2, NDVI, EVI, MNDWI, NDBI, LSWI), Sentinel-1(VV, VH), Elevation, Slope, Location	39
XGB-S1S2	2018-2019	Landsat 7-8 median, maximum, standard deviation (blue, red, green, NIR, SWIR1, SWIR2, NDVI, EVI, MNDWI, NDBI, LSWI), Sentinel-1(VV, VH), Sentinel-2(Aerosols, Water vapor, Red Edge 1-4), Elevation, Slope, Location	45

3.3 Model evaluation

Model performance is quantified by three metrics: Root Mean Square Error (RMSE, Eq. (7)), Mean Absolute Error (MAE, Eq. (8)), and coefficient of determination (R^2, Eq. (9)). Ordinary Least Squares (OLS) regression is performed to calculate the correlation between estimated and reference height values. The annual reference building height data are split into training and testing sets, utilizing 90% and 10% of the samples, respectively:

https://doi.org/10.5194/essd-2025-632
Preprint. Discussion started: 9 December 2025

Open Access Earth System Science Data Discussions

$$RMSE = \sqrt{\frac{\sum_{i=1}^{n}(H_{i,est}-H_{i,ref})^2}{n}}\ , \tag{7}$$

$$MAE = \frac{\sum_{i=1}^{n}|H_{i,est}-H_{i,ref}|}{n}\ , \tag{8}$$

$$R^2 = 1-\frac{(n-1)\sum_{i=1}^{n}(H_{i,est}-H_{i,ref})^2}{(n-2)\sum_{i=1}^{n}(H_{i,est}-H_{i,ref})^2}\ , \tag{9}$$

where n equals the number of testing samples, $H_{i,ref}$ equals the reference height value of the i-th sample point, and $H_{i,est}$ equals the estimated value.

3.4 Post process

The temporal evolution of building height at individual pixels theoretically follows a stepwise pattern: prolonged stability separated by vertical changes (construction/demolition) within a few years. However, independent annual predictions introduce arbitrary year-to-year errors unrelated to actual structural changes, causing inaccurate fluctuations within really short time periods.

To mitigate year-to-year errors, we adapt TV denoising, an approach from signal processing. Given annual sampling from 1990-2019, the height trajectory for each pixel can be interpreted as a 30-point discrete signal. TV denoising smooths these signals to preserve temporal continuity while retaining legitimate changes.

As an example of post-process, the original result before denoising in Fig.3 shows visible fluctuation between 2007 and 2008, despite minimal differences between the Landsat images from those years in Zhongguancun, Beijing. After TV denoising, the result becomes stable, aligning with the visual observation. The TV regularization parameter (λ=5) is empirically calibrated to balance noise suppression and edge preservation.

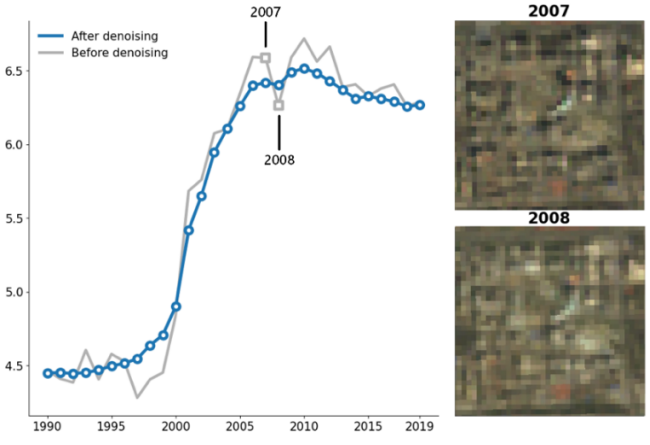

Figure 3. Effect of denoising in the sample region of Zhongguancun, Beijing. Remote sensing images are from © Google Earth.

https://doi.org/10.5194/essd-2025-632
Preprint. Discussion started: 9 December 2025

250

4 Results and discussion

4.1 Accuracy of reference samples for annual building heights

The original reference height in 2019 has a total of 5,984,743 sample pixels. After extracted by CCDC and built-up area footprints, the number of sample pixels gradually decreases each year, reaching 1,473,108 sample points by 1990 (Fig. 4). The
255 proportion of buildings of different heights also changes each year. From 2019 back to 1990, the proportion of low-rise buildings below 10 meters gradually increases, from 73.3% to 75.1%, while the proportion of mid- to high-rise buildings above 10 meters continuously decreases. The proportion of high-rise buildings between 30-60 meters and above 60 meters remains relatively small throughout. The detailed sample counts for each year are recorded in the Supplementary Table S1.

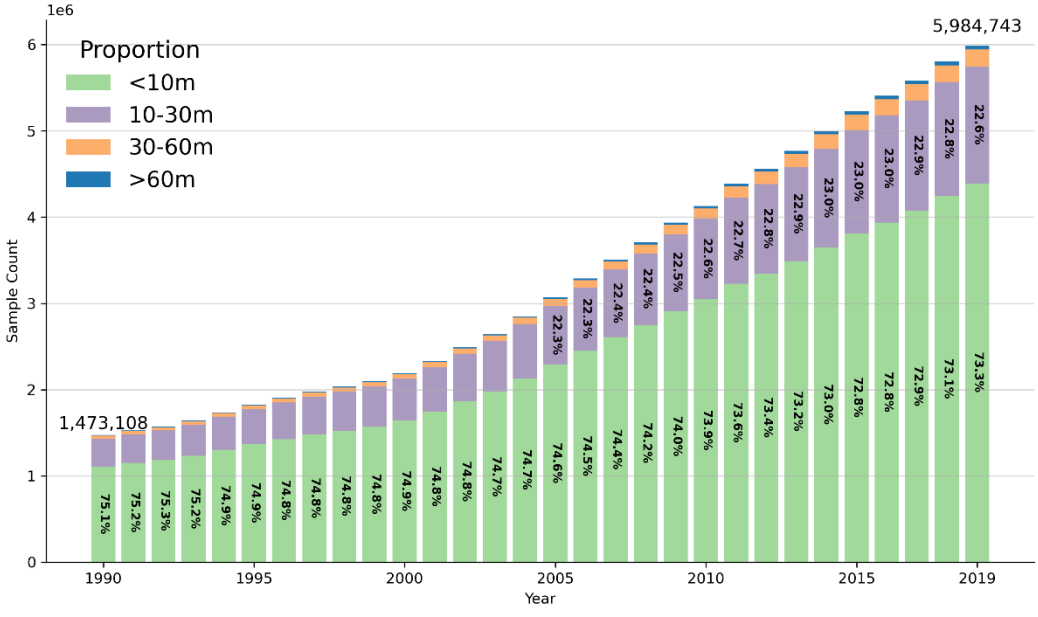

260 **Figure 4. Number of reference samples and height proportion each year.**

Housing transaction data obtained from house agent website Lianjia (https://lianjia.com) is utilized to validate the accuracy of annual samples (Wang et al., 2023). This data provides the coordinates of each transaction's community point and the community's construction year, covering 25 out of the 59 sample cities (Fig. 5c). Since a single coordinate generally correspond
265 to non-building areas such as roads, water bodies, or vegetation within a community, the CCDC breakpoint year and the settlement footprint year are set over the 3x3 pixel neighborhood around each coordinate point, and the larger value between the two are selected as the marked-up year. Only starting from the marked-up year is a sample point incorporated into the

https://doi.org/10.5194/essd-2025-632
Preprint. Discussion started: 9 December 2025

Open Access Earth System Science Data Discussions

annual reference height data, therefore sample points with their marked-up years larger than their construction years are regarded as true samples. Figure 5 demonstrates the result of validation. Most of the reference samples are extracted after the construction time, while samples around 2005 to 2015 are slightly more being incorrectly identified within a 5-year period (Fig. 5a). The accuracy gradually decreases from 2019 to 2002, eventually reaching a low point of 65.28% in 1993 after a slight increase. From 1990 to 2002, the accuracy remained around 65% (Fig. 5b). Overall, the reference samples are relatively reliable, supporting the regression process later. The exact number of validated samples and accuracy can be acquired in Supplementary Table S2.

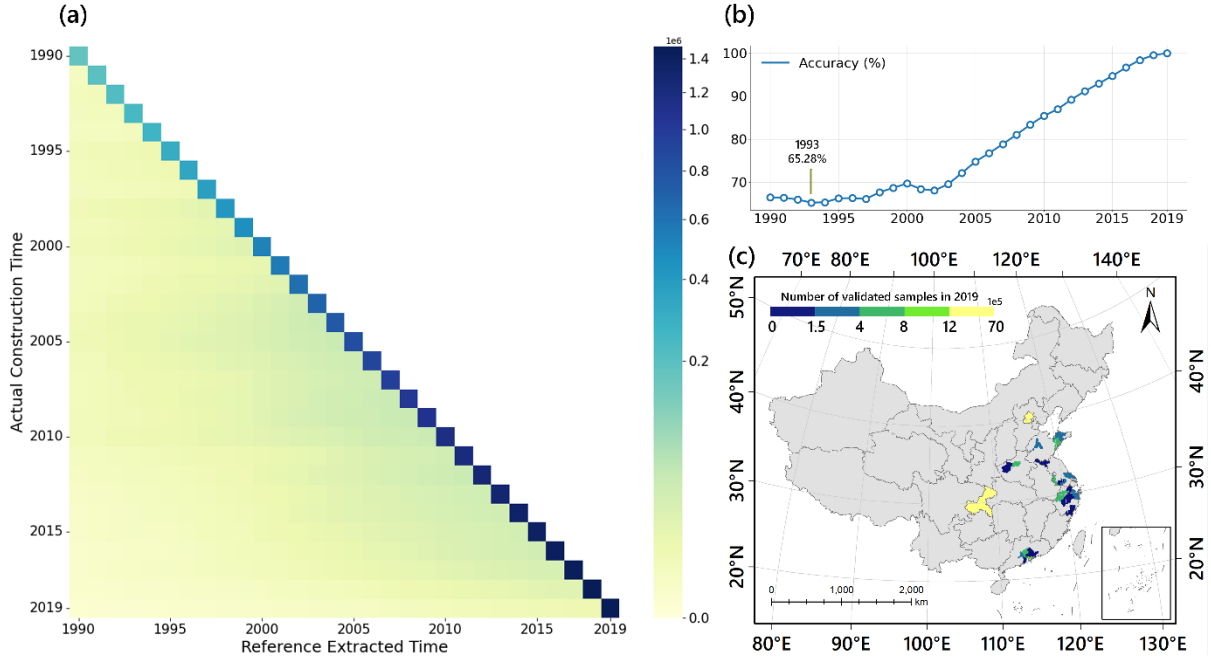

Figure 5. Results of sample validation. (a) Confusion matrix for reference time and actual construction time; (b) Accuracy of reference samples each year; (c) Number of validated samples in sampled cities.

4.2 Accuracy assessment of models

4.2.1 Performance of annual building height estimation models

Annual building height estimations show consistency with reference building heights across the research time period. From 1990 to 2019, the RMSE of XGBoost-based models (XGB-ReVV, XGB-S1 and XGB-S1S2) ranges from 5.94m to 6.69m, while the MAE varies between 3.42m and 3.81m (Fig. 6a). Accuracy indices exist a temporal progression: moving backward from 2019, both RMSE and MAE gradually increase, peaking in 2014 and 2015 respectively, and stabilizing around

https://doi.org/10.5194/essd-2025-632
Preprint. Discussion started: 9 December 2025

RMSE=6.0m and MAE=3.5m pre-2003. The error increase likely comes from limited availability of high-resolution remote sensing data sources in earlier years. The subsequent stabilization may reflect the diminishing annual reference data quantities due to CCDC masking, and decreasing proportions of high-rise buildings that cause higher estimating variations (Chen et al., 2025). The R^2 exhibits a persistent downward trajectory from 0.46 in 2019 to 0.39 in 1990 (Fig. 6b). It implies progressive degradation in the model's capacity to explain height variance using remote sensing predictors as temporal distance increases. Overall speaking, aside from the temporal tendency, the observed temporal variability in model accuracy remains constrained within modest thresholds. The peak-to-trough ratios measure 89.5% for RMSE, 91.3% for MAE and 84.7% for R^2. All metrics demonstrate sustained relative stability across the three-decade. Exact value of RMSEs, MAEs and R^2s is listed in Supplementary Table S3.

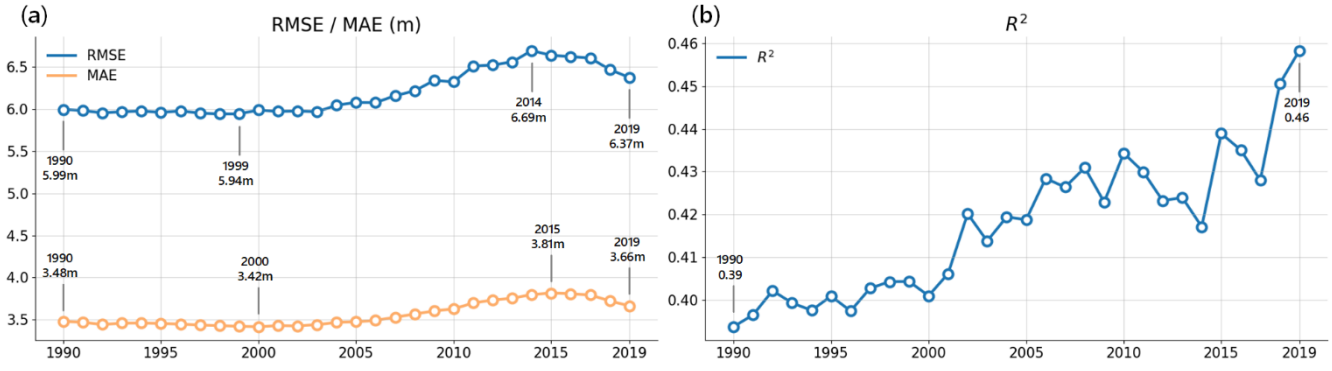

Figure 6. Model accuracy for each year. (a) the RMSE and MAE of XGBoost-based models from 1990 to 2019; (b) the R^2 of XGBoost-based models from 1990 to 2019.

The accuracy of the three XGBoost-based models is further evaluated for three representative years: 2014, 2017, and 2019 (Fig. 7). These years correspond to the initial years of XGB-ReVV, XGB-S1, and XGB-S1S2, with each model employing a distinct set of predictor variables. The prediction accuracy remains relatively consistent across these years, with RMSE values of 6.37 m, 6.60 m, and 6.69 m; MAE values of 3.66 m, 3.79 m, and 3.80 m; and R^2 values of 0.46, 0.43, and 0.42, respectively. Linear regression slopes between reference and estimated heights are 0.46, 0.45, and 0.46, with intercepts of 1.20 m, 1.25 m, and 1.23 m. The minimal intercepts indicate negligible baseline offsets for low-rise structures. The slopes confirm systematic underestimation of high-rise buildings, with predictions approximating 50% of actual values. This problem is stressed in multiple previous studies (Frantz et al., 2021; Che et al., 2024; Cao and Weng, 2024). Height-stratified analysis reveals differential performance: predictions for sub-10m buildings demonstrate high accuracy, while 10-30 m structures show prevalent underestimation. Moderate accuracy is observed for 30-60 m buildings, with most estimations being accurate while a lower error peak exists at around 30 m. High-rise structures exceeding 60 m exhibit underestimation, consistent with the

https://doi.org/10.5194/essd-2025-632
Preprint. Discussion started: 9 December 2025

regression-derived slope patterns. The results from linear regression and height-stratified analysis for each year from 1990 to 2019 are presented in Supplementary Fig. S1 and S2.

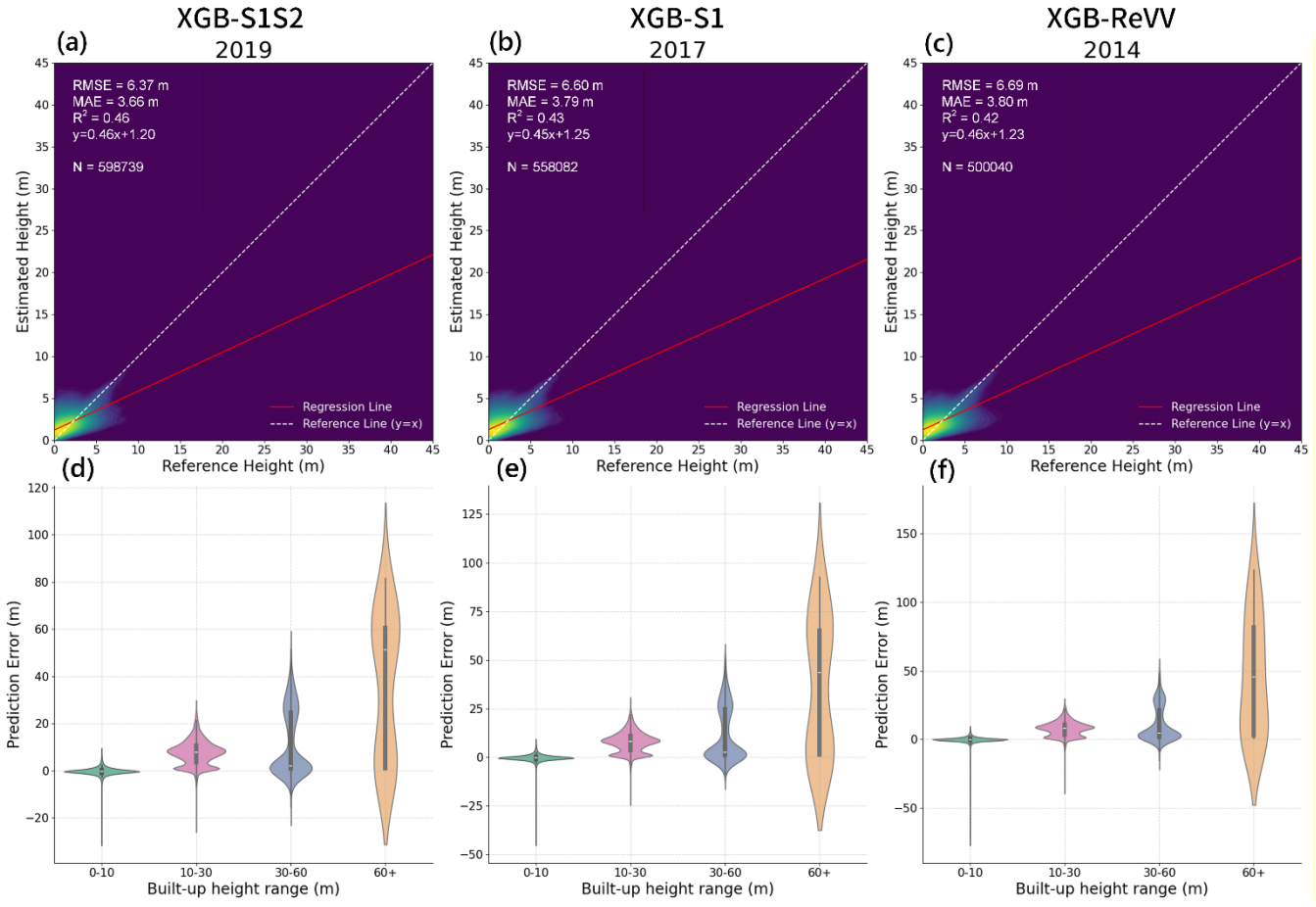

315 **Figure 7. Accuracy of XGBoost-based models in their initial years.** (a, d) XGB-S1S2 (2019); (b, e) XGB-S1 (2017); (c, f) XGB-ReVV (2014).

4.2.2 Spatial distribution of accuracy indices

Significant regional discrepancies in prediction accuracy are observed across the 59 training cities using the 2019 model. A distinct north-south performance difference emerges (Fig. 8). Northern cities such as Beijing (RMSE=3.18m, MAE=2.16m,
320 R^2=0.82) and Xi'an (RMSE=4.75m, MAE=2.78m, R^2=0.71) show better performances than average metrics, while southern counterparts like Changsha (RMSE=6.11m, MAE=3.27m, R^2=0.43) barely approach the mean values, and Nanchang (RMSE=7.57m, MAE=4.58 m, R^2=-0.56) significantly underperform. Cities in the Pearl River Delta exhibit particularly low accuracy, with Hong Kong (RMSE=7.55m, MAE=3.28 m, R^2=0.71), Guangzhou (RMSE=11.86 m, MAE=7.32 m, R^2=-1.41),

https://doi.org/10.5194/essd-2025-632
Preprint. Discussion started: 9 December 2025

and Foshan (RMSE=11.66 m, MAE=7.37 m, R^2=-1.66). These regional disparities may be attributed to meteorological factors—frequent cloud cover and precipitation in southern China likely degraded optical remote sensing data quality, thereby introducing noise into the prediction models (Zhang and Weng, 2016). Accuracy assessments for each training-sample city for every year from 1990 to 2019 are recorded in Supplementary Table S4.

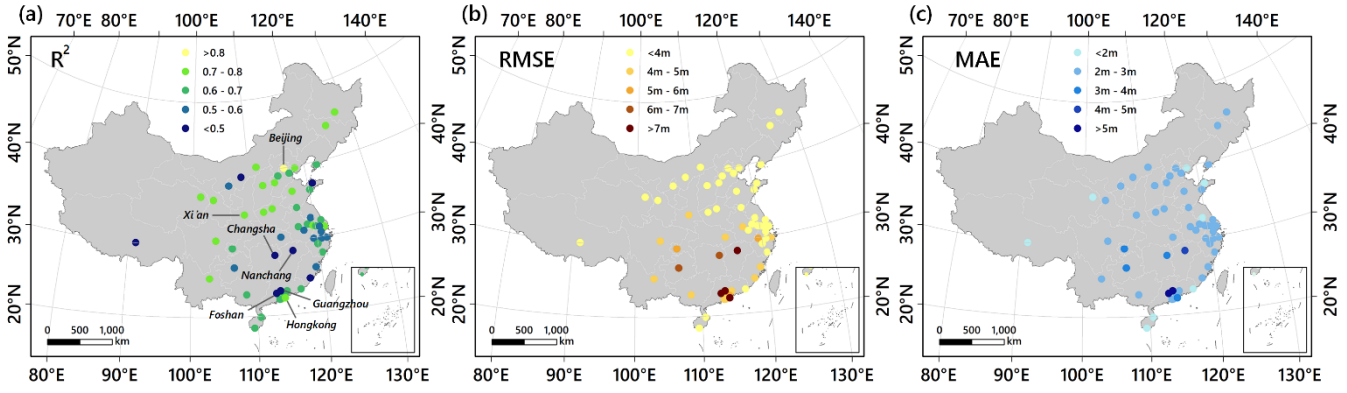

Figure 8. Distribution of accuracy indices across cities in 2019. (a) RMSE; (b) MAE; (c) R^2.

4.3 The importance of variables

To evaluate the contributions of different variables derived from multi-source remote sensing imagery, predictor importance is quantified for three representative years: 2014, 2017, 2019. Correspondingly, XGB-ReVV, XGB-S1, and XGB-S1S2 are trained for these years. (Fig. 9a). For Landsat bands and derived indices represented by three temporal composites (maximum, median, standard deviation), the mean importance of these composites is calculated per spectral feature. Geographic coordinates demonstrate the highest predictive importance, with latitude achieving values of 0.091, 0.120, and 0.133 across the three years, and longitude reaching 0.061, 0.071, and 0.086. Sentinel-2 spectral bands exhibit moderate contributions: Red Edge 4 (0.047), Aerosol (0.033), Red Edge 1 (0.022), and Water Vapor (0.021). In radar data, Sentinel-1's VH polarization show higher importance (0.042 in 2019, 0.040 in 2017) compared to VV (0.020 and 0.019). After replacing with reconstructed 1km VV backscatter, its importance is 0.019. DEM elevation (0.027, 0.030, 0.022) maintains consistent relevance across the years. In conclusion, location variables (latitude/longitude) dominate predictive capacity, followed by Sentinel-1 VH backscatter, DEM elevation, and selected optical bands including Sentinel-2 Red Edge 1/Aerosols alongside Landsat Green/NIR. Despite optical sensors providing numerous spectral variables, most exhibit limited individual importance.

The role of reconstructed 1km-resolution VV backscatter is further investigated in height prediction accuracy. RMSE differences are compared between models incorporating and excluding this variable for 1990-2014 predictions on the same test set (Fig. 9b). For low- to mid-rise buildings (<30m), models with reconstructed VV shows marginally lower RMSE, while mid-rise structures (30-60m) exhibit slightly higher accuracy without VV integration. The most significant divergence occurrs in high-rise predictions (>60m). Although inherently prone to larger errors, high-rise estimations demonstrate measurable improvements with reconstructed VV inclusion—particularly in 2005 and 2010, where RMSE decreases from 64.81 m and

https://doi.org/10.5194/essd-2025-632
Preprint. Discussion started: 9 December 2025

54.61 m (without VV) to 44.20 m and 34.46 m (with VV), respectively. This indicates that despite low variable importance rankings, reconstructed VV meaningfully enhances vertical discrimination capacity for high-rise buildings.

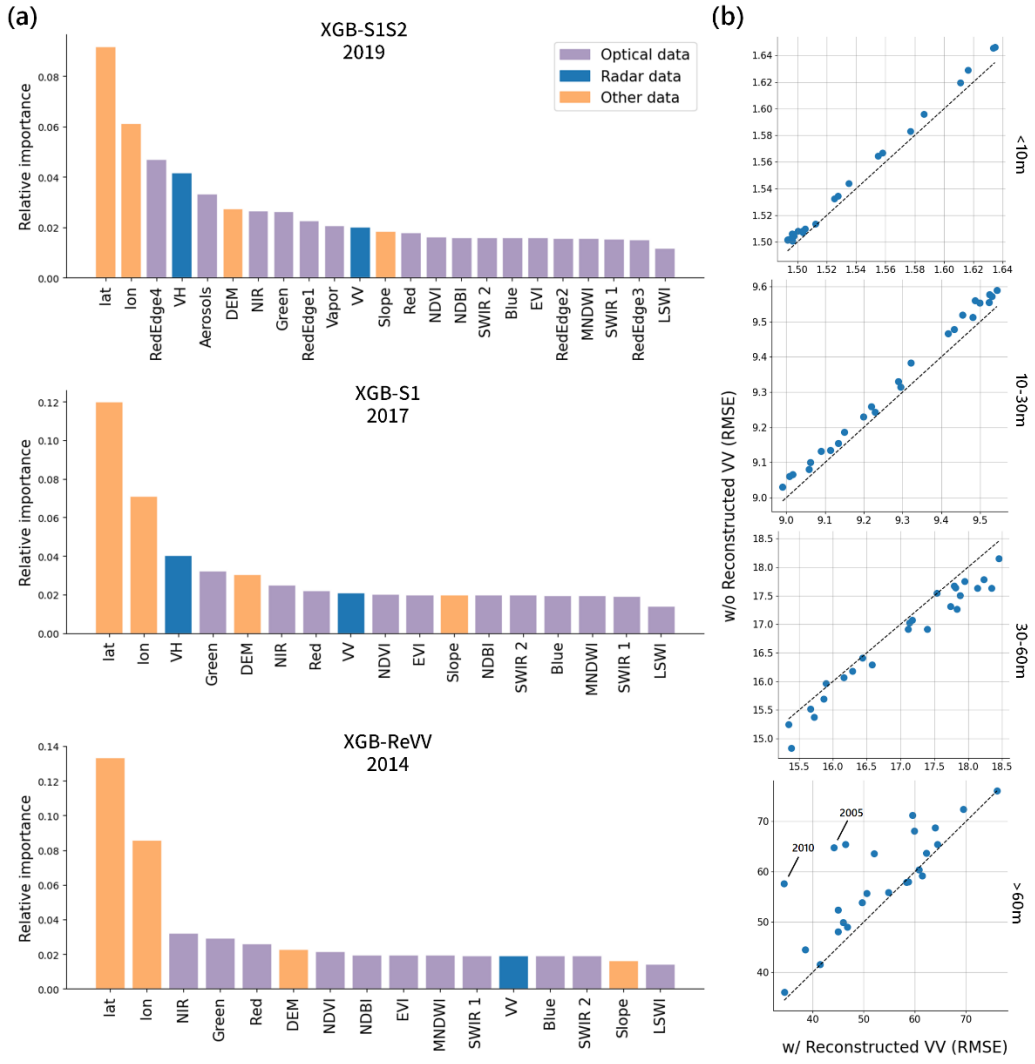

Figure 9. Importance evaluation of variables. (a) Relative importance of different variables; (b) RMSE differences between models with and without reconstructed VV.

4.4 Comparison with existing building height datasets

4.4.1 Comparison with single-year building height datasets

To demonstrate the quality of the long-term building height dataset, it is compared with other existing pixel-level products (Fig. 10). Beijing is selected as the comparative study area due to its complex urban morphology and heterogeneous building

https://doi.org/10.5194/essd-2025-632
Preprint. Discussion started: 9 December 2025

height distribution, serving as a representative validation zone for height dataset evaluation. Wu's (Wu et.al., 2023), WSF 3D (Esch et al., 2023) and Ma's (Ma et al., 2024) single-year datasets are quantified as benchmarks (Table 3). All these datasets are constructed through conventional machine learning approaches at the pixel level, and are derived based on reference height data in 2019. Therefore, they exhibit strong methodological comparability with our product. Since each dataset has a different resolution, for WSF 3D and Ma's, the reference height is resampled to corresponding resolution. For Wu's, it is downsampled to 30m to fit the corresponding resolution of reference heights.

Table 4. Datasets selected for the single-year comparison

Dataset	Year	Resolution	Source
WSF 3D (Esch et al., 2022)	2019	90m	https://download.geoservice.dlr.de/WSF3D/files/
CNBH-10m (Wu et al., 2023)		10m	https://zenodo.org/records/7923866
Ma's dataset (Ma et al., 2024)		150m	https://figshare.com/articles/dataset/2020_150__/25729248/6?file=49885077
Our dataset	1990-2019	30m	https://doi.org/10.6084/m9.figshare.29918978

The results show our dataset have a good agreement with the reference dataset, with RMSE at 4.04m, slightly higher than the height of a single floor, and MAE at 2.66m (Fig. 10b). Wu's, WSF 3D and Ma's datasets expose visible biases, with RMSE differing from 6.69m to 748.79m and MAE differing from 4.61m to 69.54m (Fig. 10c-e). Our dataset holds less underestimation compared to other datasets, while all these datasets express a tendency to underestimate the height of high-rise buildings. Distribution of building heights in our dataset each year from 1990 to 2019 is recorded in Supplementary Fig. S3.

https://doi.org/10.5194/essd-2025-632
Preprint. Discussion started: 9 December 2025

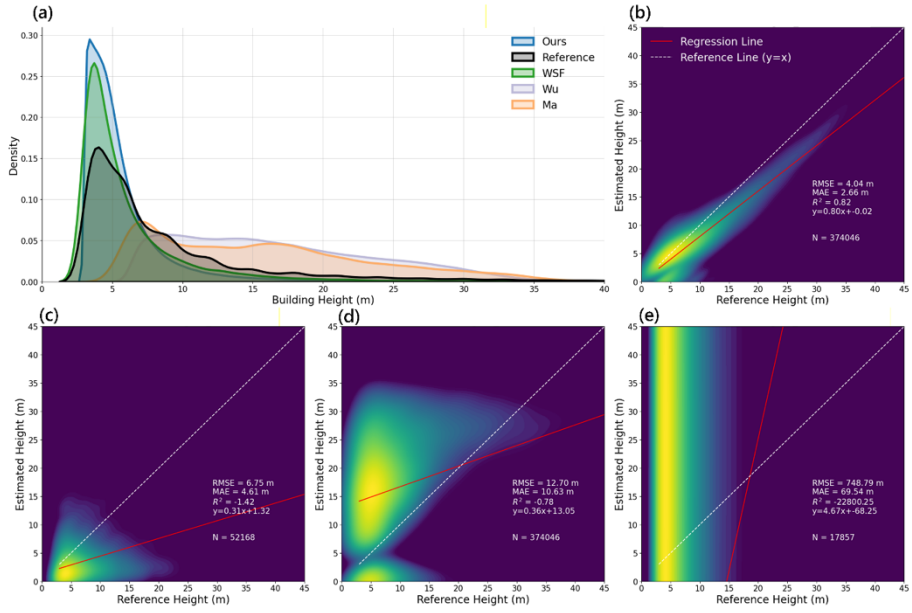

Figure 10. Comparsion of reference height, our dataset and other datasets in 2019. (a) Height distribution of different datasets; (b) Scatter plot of our dataset and reference heights; (c) Scatter plot of WSF 3D (Esch et al., 2022) and reference heights; (d) Scatter plot of CNBH-10m (Wu et al., 2023) and reference heights; (e) Scatter plot of Ma's dataset (Ma et al., 2024) and reference heights.

Four major Chinese cities, Beijing, Shanghai, Chengdu, and Guangzhou, are selected for qualitative evaluation across datasets (Fig.11). Visual comparisons reveal that our dataset and WSF 3D closely approximate reference height distributions in all cities. In Beijing, Shanghai, and Chengdu, where building heights exhibit significant variability, the Wu's and Ma's datasets systematically overestimate vertical structures. In contrast, Guangzhou's predominantly high-rise urban morphology shows better alignment with Wu's and Ma's estimates, while WSF 3D underestimates heights. Our dataset successfully resolves this regional discrepancy, accurately capturing Guangzhou's high-density vertical urban growth alongside other cities' height heterogeneities.

https://doi.org/10.5194/essd-2025-632
Preprint. Discussion started: 9 December 2025

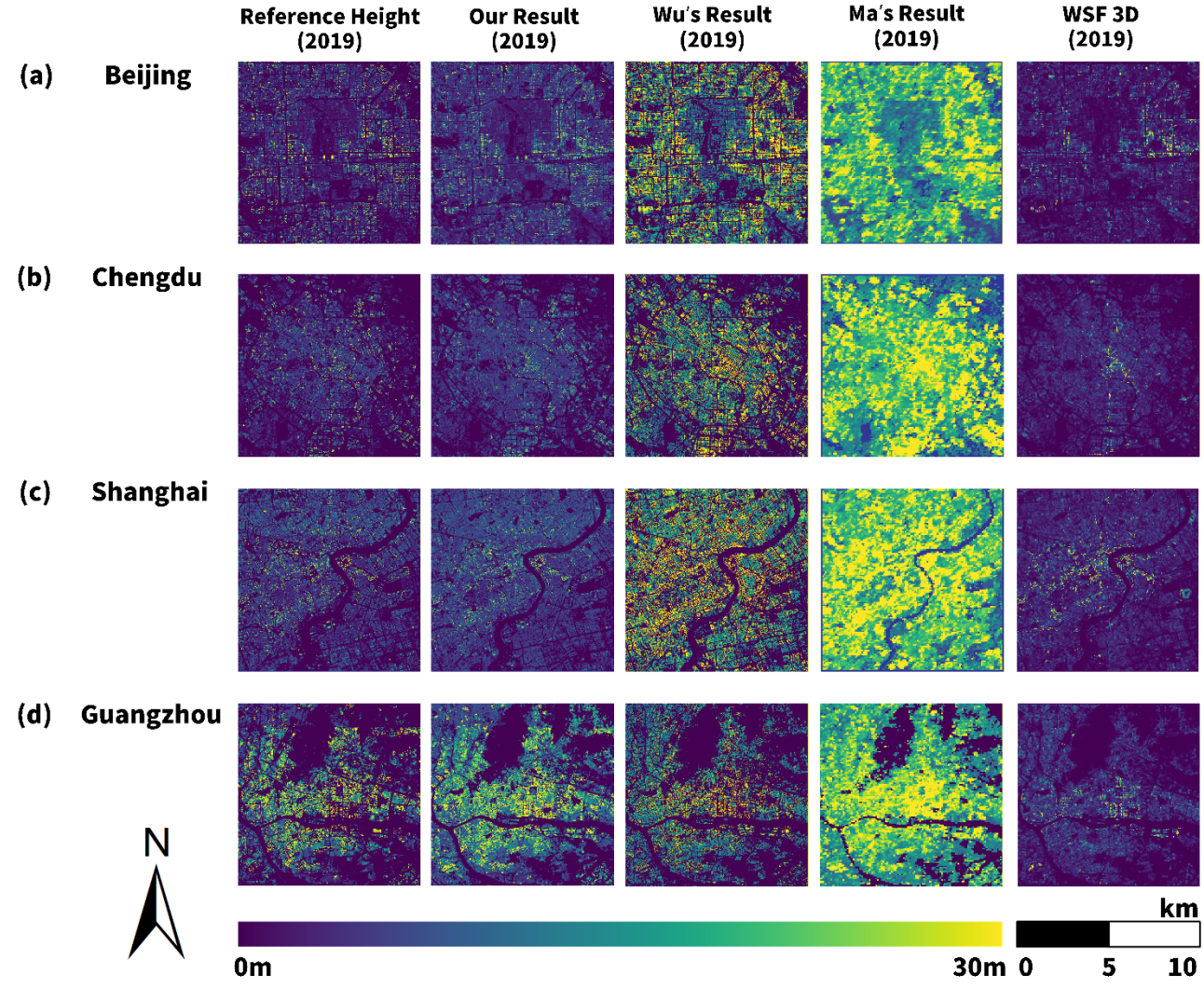

Figure 11. Comparison of building height datasets in different cities. (a) Beijing; (b) Chengdu; (c) Shanghai; (d) Guangzhou.

4.4.2 Comparison with long-term building height products

To give out a comprehensive comparison with existing long-term building height products, two long-term building height datasets are selected for analysis (Table 4): He's dataset (He et al., 2023) and China Multi-Attribute Building (CMAB) dataset (Zhang, Zhao and Long, 2025). While CMAB records footprint-level attributes including height, structure, function, style, age, and quality, this study exclusively utilizes its height and age components. Both He's dataset and CMAB document building construction completion years, therefore average building height of each reference year is calculated by considering all the buildings constructed before the given year. For our dataset, direct annual height averaging is implemented. Figure 12

https://doi.org/10.5194/essd-2025-632
Preprint. Discussion started: 9 December 2025

compares annual mean height trends across the three datasets. Median values, Q1/Q3 quartiles, and 1.5×standard deviation ranges comprehensively characterize height distributions.

The results reveal that average building heights remain stable between 1990 and 2019 across our dataset, He's and CMAB. Our dataset and He's both maintain mean heights of about 7 m, while CMAB reports higher values above 14 m. The higher CMAB values result from its focus on urban centers, whereas the other datasets also include rural and township areas. All datasets underestimate structural heights due to pixel-scale averaging of buildings within 30 m grids (Eq. 6). This nationwide stability suggests an urban development trajectory in China balancing horizontal expansion with vertical growth. Section 4.5 further examines the relationship between horizontal sprawl and vertical increase. The detailed value of annual mean height for our dataset is recorded in Supplementary Table S5.

Table 5. Datasets selected for the long-term comparison

Dataset	Year	Resolution	Source
He's (Esch et al., 2022)	2010	30m	https://doi.org/10.6084/m9.figshare.21792209.v2
CMAB (Zhang, Zhao and Long, 2025)	2023	Vector	https://doi.org/10.6084/m9.figshare.27992417.v2
Our dataset	1990-2019	30m	https://doi.org/10.6084/m9.figshare.29918978

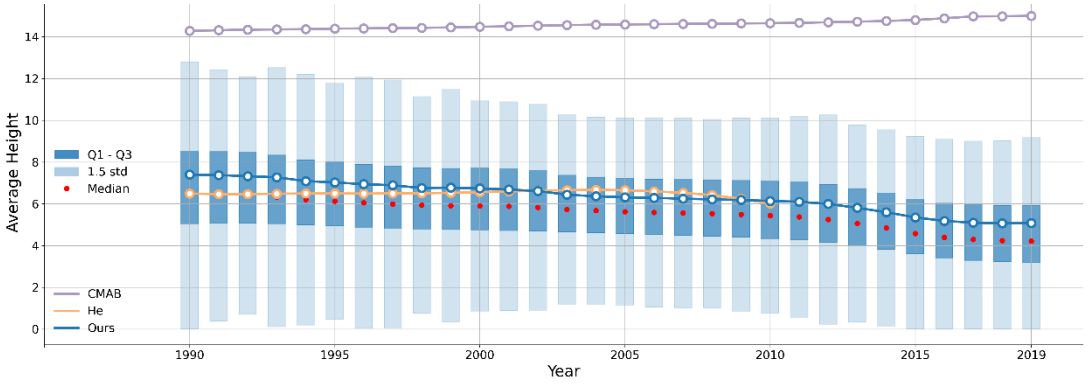

Figure 12. Temporal change in annual average height in three long-term building height datasets.

4.4.3 Comparison with historical remote sensing images

The accuracy of the dataset is further validated through comparisons between the mapped estimates and visual evidence from historical remote sensing imagery. Six representative areas are selected for evaluation: three included in training-set cities—Tianjin, Beijing, and Wuhan (Fig. 13a–c)—and three included in non-training-set cities—Handan, Jining, and Anyang (Fig.

https://doi.org/10.5194/essd-2025-632
Preprint. Discussion started: 9 December 2025

14a–c). The mapped results in the training-set cities exhibit close agreement with urban changes recorded in the imagery. In the non-training-set cities, although the detailed building contours are less distinct, construction and demolition activities remain clearly identifiable. More specifically:

(1) In Tianjin Drum Tower (Region 1, Fig. 13a), bungalows are demolished around 2001 and redeveloped into apartment buildings, which is evident in the 2005 and 2010 imagery. By 2019, a notable increase in high-rise structures becomes visible.

(2) In Beijing Jiaohuachang (Region 2, Fig. 13b), the high-rise coke plant visible in 2005 is removed by 2010 and replaced with a subway garage, which appears clearly in the 2018 imagery.

(3) In Wuhan Yijianyuan (Region 3, Fig. 13c), farmland present in 2000 is converted into impervious surfaces by 2005, followed by continuous high-rise development that becomes increasingly evident in the 2013 and 2019 imagery.

(4) In Handan Congtai Park (Region 1, Fig. 14a), a similar redevelopment pattern to that in Tianjin is observed. The area remains dominated by bungalows in 2006 but is gradually transformed into clusters of multi-story apartments, which are prominent in the 2013 and 2019 imagery.

(5) In Jining Shiliying Village (Region 2, Fig. 14b), the entire settlement progressively sinks into a subsidence lake, causing the gradual abandonment and demolition of houses and resulting in the village's near disappearance by 2019 in both the satellite imagery and our dataset.

(6) In Anyang Yiyuan (Region 3, Fig. 14c), completely new developments are established on previously undeveloped land, becoming increasingly extensive between 2005 and 2019.

These visual comparisons collectively provide additional evidence that the dataset effectively captures diverse patterns of urban growth and renewal across regions with different development trajectories.

https://doi.org/10.5194/essd-2025-632
Preprint. Discussion started: 9 December 2025

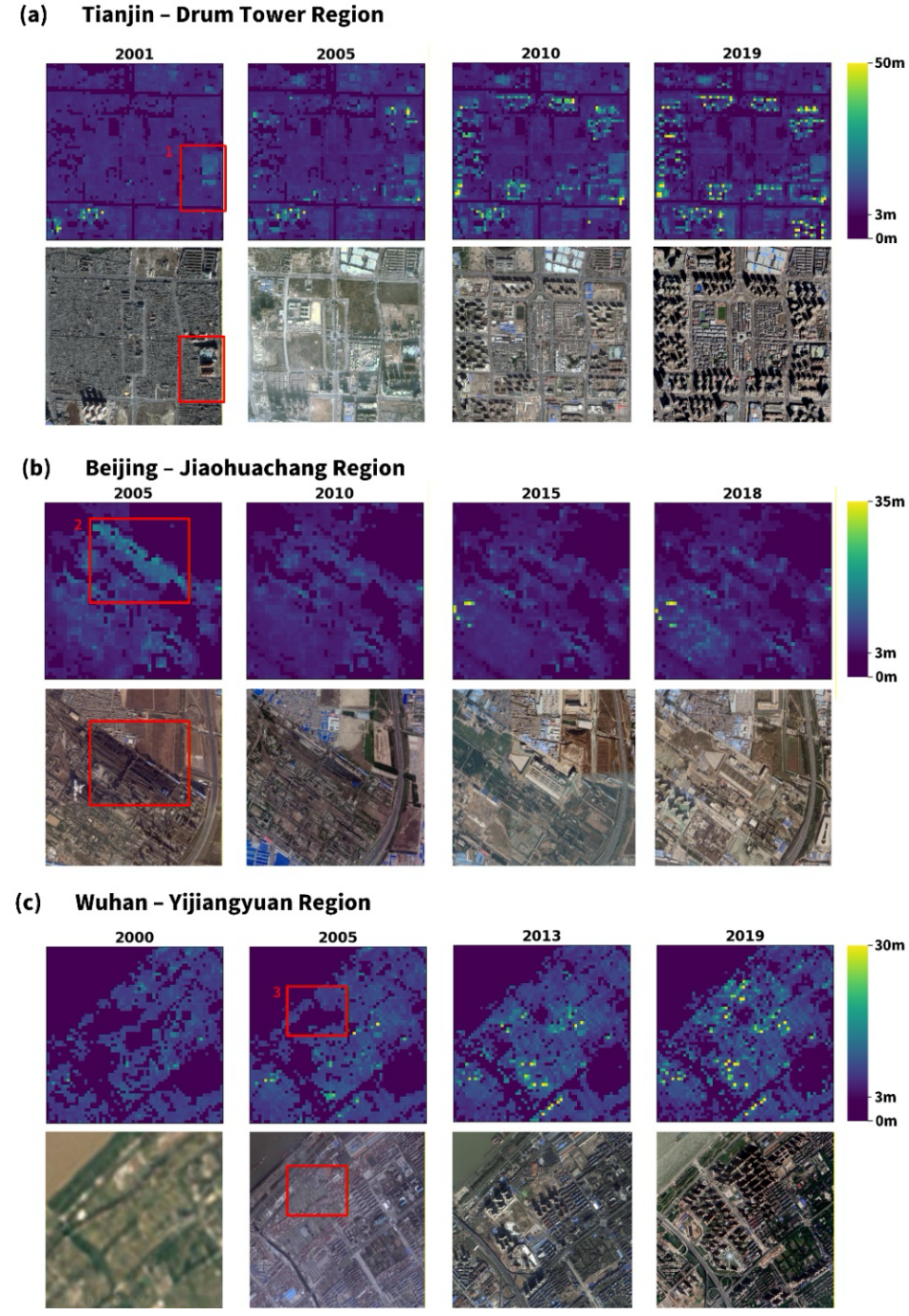

435 **Figure 13. Comparison of urban areas in sampled cities using Google historical remote sensing images.** (a) Drum Tower region, Tianjin; (b) Jiaohuachang region, Beijing; (c) Yijiangyuan region, Wuhan. Remote sensing images are from © Google Earth.

https://doi.org/10.5194/essd-2025-632
Preprint. Discussion started: 9 December 2025

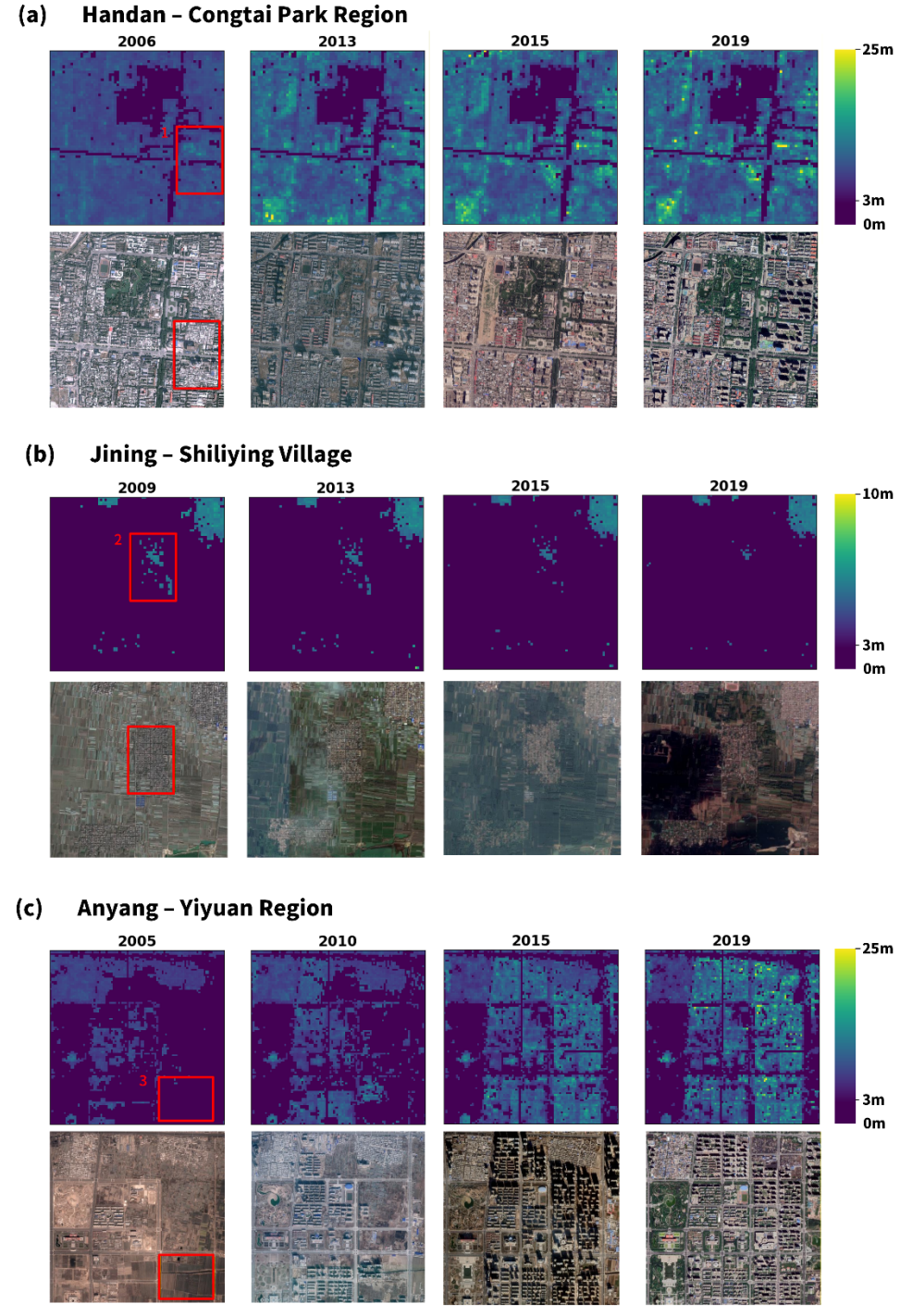

Figure 14. Comparison of urban areas in non-sampled cities using Google historical remote sensing images. (a) Congtai Park region, Handan; (b)Shiliying region, Jining; (c) Yiyuan region, Anyang. Remote sensing images are from © Google Earth.

https://doi.org/10.5194/essd-2025-632
Preprint. Discussion started: 9 December 2025

4.5 Mapping of annual Chinese building heights

4.5.1 Dynamic of building height

As the start and end years of our dataset, 1990 and 2019 are selected to illustrate China's building height distributions (Fig. 15a, b). Given the large data volume, visualizations are aggregated to 1 km resolution for national-scale representation. During this period, urban built-up areas expanded substantially, accompanied by a clear increase in building heights. This trend is most pronounced on the North China Plain and in fast-growing metropolitan regions of central and eastern China.

City-level temporal visualization for Shanghai, Beijing and Shenzhen (Fig. 15c-e) depict their urbanization trajectories in 1990, 2000, 2010, and 2019. Core urban areas maintain relatively stable building heights, with only incremental additions of high-rise structures in all three cities. Peripheral districts undergo rapid land conversion and construction, resulting in taller and denser building clusters over time. For example, in Shenzhen, Luohu District had the tallest skyline in 1990, while Futian District experienced concentrated development after 2000, eventually surpassing Luohu in building height and density.

https://doi.org/10.5194/essd-2025-632
Preprint. Discussion started: 9 December 2025

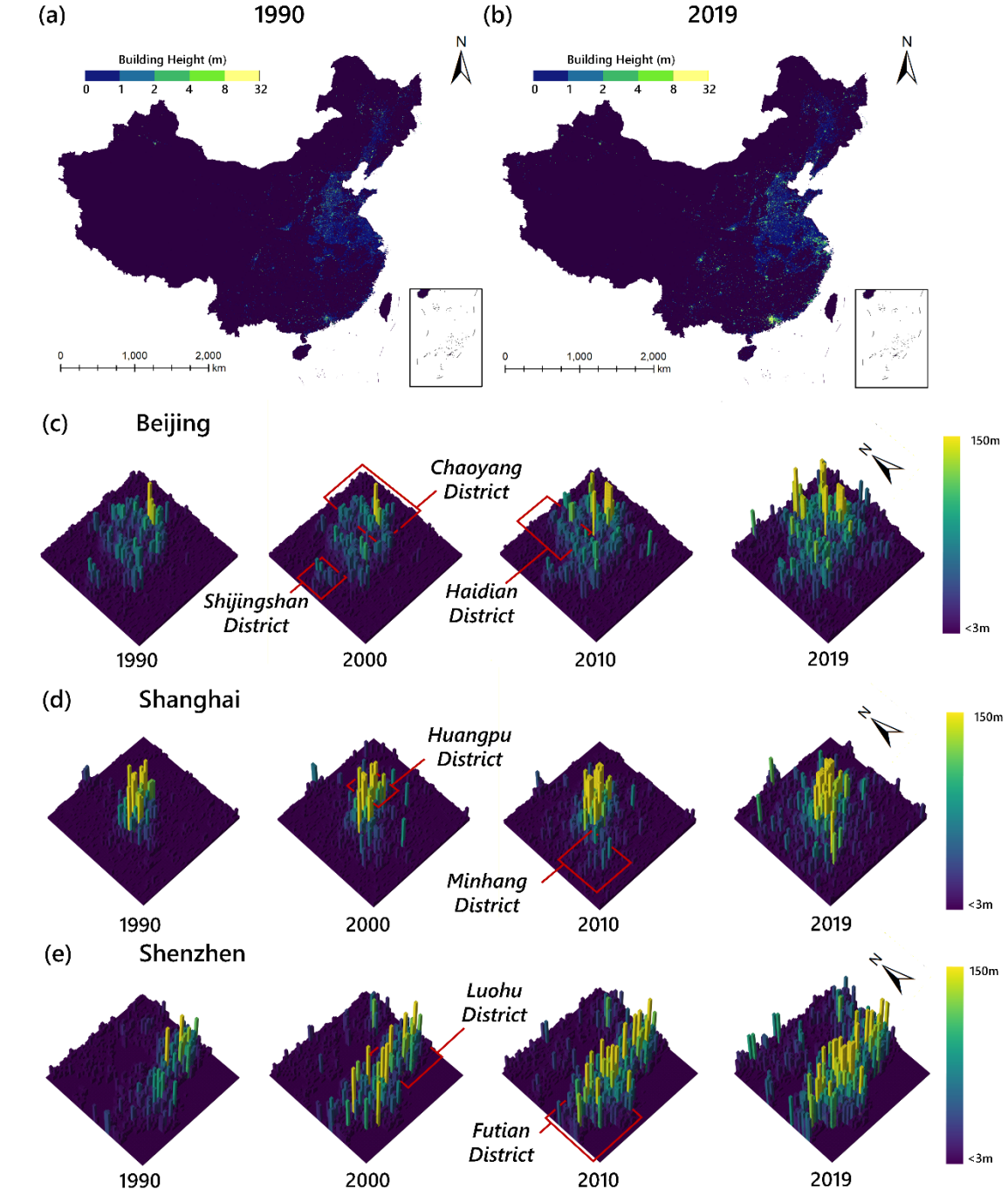

455 **Figure 15. Spatial distribution and temporal progression of building heights.** (a, b) Spatial distribution of building heights in 1990 and 2019; (c-e) Temporal progression of building height in Beijing, Shanghai and Shenzhen.

https://doi.org/10.5194/essd-2025-632
Preprint. Discussion started: 9 December 2025

4.5.2 Dynamic of building volume

Our dataset presents a consistent depiction of both horizontal and vertical expansion of the built environment across China from 1990 to 2019, accurately capturing nationwide urban growth over the past three decades. During this period, total building volume increased markedly from 471.24 km³ in 1990 to 884.69 km³ in 2019, while total impervious surface area expanded from 56,413.68 km² to 174,320.66 km².

Figure 16a and 16b illustrate widespread volumetric growth across almost all provinces, despite the pronounced regional heterogeneity. By 2019, national building volume reaches approximately 884.49 km³, which is generally consistent with GlobalBuildingAtlas estimates (approximately 700 km³; Zhu et al., 2025). At the city scale, our estimates display strong agreement with 3D-GloBFP (Che et al., 2024), such as Beijing (ours: 16.4 km³ vs. 13 km³) and Shanghai (ours: 12.6 km³ vs. 14.1 km³).

Figure 16c and 16d further show shifting contributions to national building volume. In 1990, Hebei (12.9%), Shandong (11.4%), and Henan (10.3%) were the largest contributors. By 2019, Shandong remains the highest (10.0%), while coastal provinces such as Guangdong (9.5%) and Jiangsu (8.0%) gain substantially in their share, indicating accelerated coastal urbanization driven by economic growth.

Figure 16e–g reveal the temporal trajectories of total building volume, impervious surface area, and mean building height. Although the mean building height exhibits a slight declining trend after 1990, indicating that outward expansion slightly outpaces vertical increase, both building volume and impervious surface area continue to increase. The growth rate of building volume begins to slow around 2016 and approaches a relatively stable level by 2019. For impervious surface area, a decline in growth rate occurs after 2016, with subsequent increases remaining relatively modest. Annual values for these indicators are provided in Supplementary Table S5.

https://doi.org/10.5194/essd-2025-632
Preprint. Discussion started: 9 December 2025

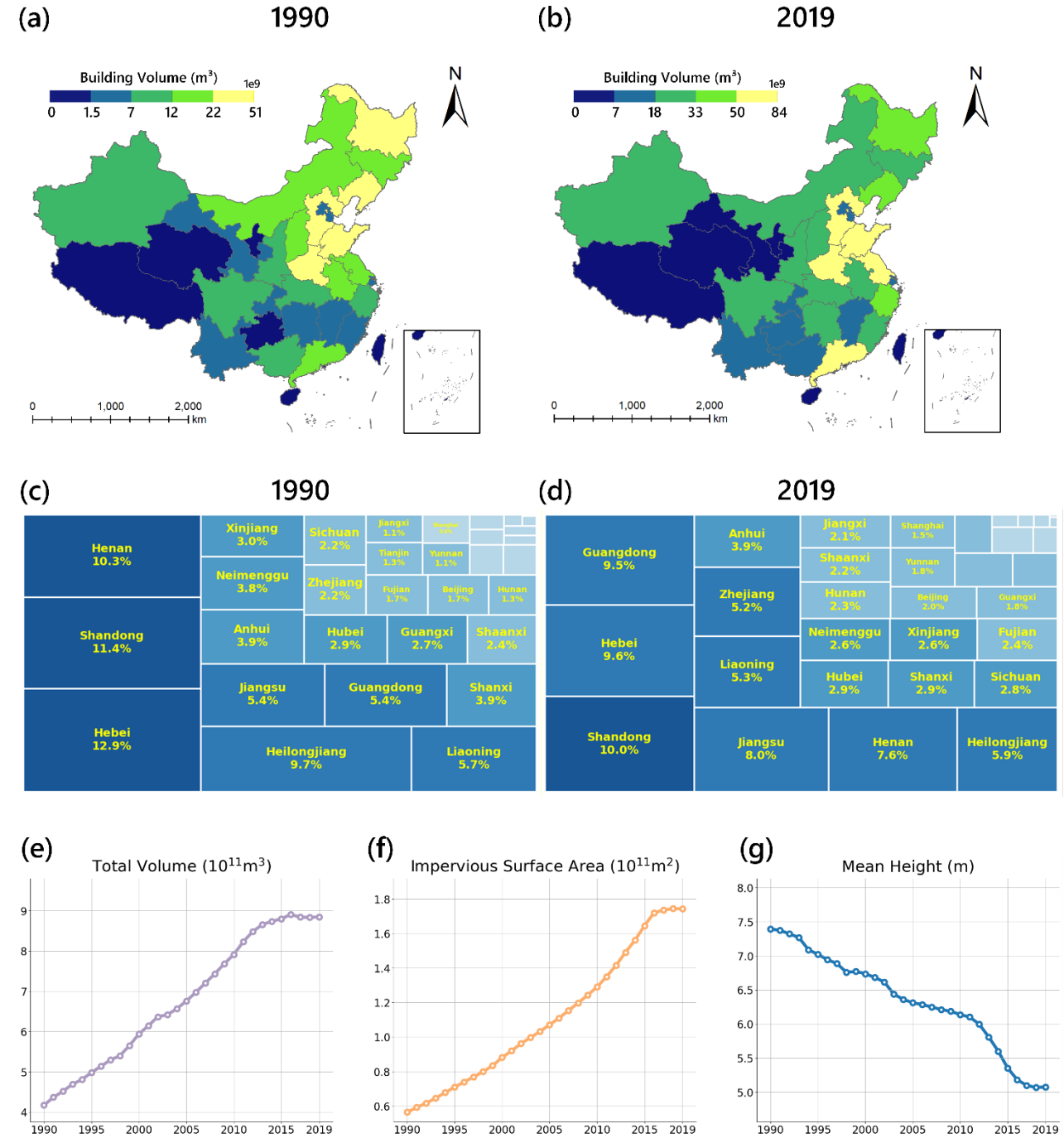

Figure 16. Spatial distribution and temporal progression of building volume, impervious surface area and mean building height. (a, b) Spatial distribution of building volume in 1990 and 2019; (c, d) Share of building volume of each province of China; (e-g) Temporal progression of building volume, impervious surface area and mean building height.

https://doi.org/10.5194/essd-2025-632
Preprint. Discussion started: 9 December 2025

Open Access Earth System Science Data Discussions

5 Data availability

Data described in this manuscript can be accessed at https://doi.org/10.6084/m9.figshare.29918978 (Zhang et al., 2025). The dataset is stored in TIF format. Each image covers a 2°×2° area, with its name representing the lower left longitude and latitude of the region. Each image has 30 bands, from the first band storing building height data of 2019, to the last band of 1990.

6 Conclusion and future work

The first long-term, continuous annual building height dataset for China from 1990 to 2019 at 30 m resolution is established through the integration of multi-source and multi-temporal remote sensing data with machine learning. By reconstructing SAR backscatter, applying CCDC-based reference data, and incorporating TV denoising, the dataset maintains year-to-year consistency and captures inter-annual variations in building heights. Accuracy assessments indicate high precision and stable performance over three decades, with RMSE ranging from 5.96 to 6.69 m, MAE from 3.42 to 3.81 m, and R^2 between 0.39 and 0.46, despite the reduced availability of high-resolution variables in earlier years. In addition, our dataset demonstrates higher accuracy in Beijing for 2019 compared to that of Wu et al. (2023), reducing the RMSE from 12.7 m to 4.04 m. Validation against existing building height products and historical remote sensing images further demonstrates its reliability and generalizability, ensuring broad applicability for both national and localized urban morphology analyses. Moreover, our dataset reveals that both built-up area and building volume continue to expand nationwide from 1990 to 2019. Meanwhile, the contributions of different provinces to the national building volume vary considerably over time, reflecting heterogeneous urban development trajectories across regions. As land resources become increasingly constrained and population increases, the developmental paradigm shifts from increment to stock (Frolking et al., 2024; Li, 2016). Future trajectories are likely to involve more intensive use of vertical space within relatively stable built-up footprints. Under this scenario, the mean building height of built-up areas continues to rise, marking a transition from land-extensive growth to space-efficient densification. Extending the current framework to construct forward-looking datasets that project such trajectories represents a critical direction, offering opportunities to anticipate future morphological change and support urban sustainability planning.

Supplement

Supplementary material includes 4 figures and 5 tables.

https://doi.org/10.5194/essd-2025-632
Preprint. Discussion started: 9 December 2025

Author contribution

YZ: Conceptualization, Data curation, Investigation, Methodology, Software, Visualization, Writing (original draft preparation), Writing (review and editing). **YW:** Investigation, Methodology, Validation, Writing (review and editing). **QD:** Conceptualization, Formal analysis, Funding acquisition, Investigation, Methodology, Writing (review and editing). **XC:** Formal analysis, Validation. **FZ:** Funding acquisition, Project administration, Supervision. **XL:** Conceptualization, Methodology, Writing (review and editing). **YL:** Resources, Supervision.

Competing interests

At least one of the (co-)authors is a member of the editorial board of Earth System Science Data.

References

Alahmadi, M., Atkinson, P., and Martin, D.: Estimating the spatial distribution of the population of Riyadh, Saudi Arabia using remotely sensed built land cover and height data, Computers, Environment and Urban Systems, 41, 167-176, https://doi.org/10.1016/j.compenvurbsys.2013.06.002, 2013

Cao, Y., and Weng, Q.: A deep learning-based super-resolution method for building height estimation at 2.5 m spatial resolution in the Northern Hemisphere, Remote Sensing of Environment, 310, 114241, https://doi.org/10.1016/j.rse.2024.114241 ,2024

Che, Y., Li, X., Liu, X., Wang, Y., Liao, W., Zheng, X., Zhang, X., Xu, X., Shi, Q., Zhu, J., Yuan, H., and Dai, Y.: 3D-GloBFP: The first global three-dimensional building footprint dataset, Earth System Science Data Discussions, 2024, 1-28, https://doi.org/10.5194/essd-2024-217, 2024

Chen, P., Huang, H., Qin, P., Liu, X., Wu, Z., Zhao, F., Liu, C., Wang, J., Li, Z., Cheng, X., and Gong, P.: Characterizing dynamics of built-up height in China from 2005 to 2020 based on GEDI, Landsat, and PALSAR data, Remote Sensing of Environment, 325, 114776, https://doi.org/10.1016/j.rse.2025.114776, 2025

Chen, T., and Guestrin, C.: XGboost: A scalable tree boosting system. In Proceedings of the 22nd acm sigkdd international conference on knowledge discovery and data mining (pp. 785-794), https://doi.org/10.1007/978-3-031-63219-8_5, 2016

Cohen, B.: Urbanization, City growth, and the New United Nations development agenda, Cornerstone, 3(2), 4-7, https://doi.org/10.3197/jps.63799977346495, 2015

Esch, T., Brzoska, E., Dech, S., Leutner, B., Palacios-Lopez, D., Metz-Marconcini, A., Marconcini, M., Roth, A., and Zeidler, J.: World Settlement Footprint 3D-A first three-dimensional survey of the global building stock, Remote sensing of environment, 270, 112877, https://doi.org/10.1016/j.rse.2021.112877, 2022

https://doi.org/10.5194/essd-2025-632
Preprint. Discussion started: 9 December 2025

Frantz, D., Schug, F., Okujeni, A., Navacchi, C., Wagner, W., van der Linden, S., and Hostert, P.: National-scale mapping of building height using Sentinel-1 and Sentinel-2 time series, Remote Sensing of Environment, 252, 112128, https://doi.org/10.1016/j.rse.2020.112128, 2021

Frantz, D., Schug, F., Wiedenhofer, D., Baumgart, A., Virág, D., Cooper, S., Gómez-Medina, C., Lehmann, F., Udelhoven, T., van der Linden, S., Hostert, P., and Haberl, H.: Unveiling patterns in human dominated landscapes through mapping the mass of US built structures, Nature Communications, 14(1), 8014, https://doi.org/10.1038/s41467-023-43755-5, 2023

Frolking, S., Milliman, T., Mahtta, R., Paget, A., Long, D. G., and Seto, K. C.: A global urban microwave backscatter time series data set for 1993–2020 using ERS, QuikSCAT, and ASCAT data, Scientific Data, 9(1), 88, https://doi.org/10.1038/s41597-022-01193-w, 2022

Frolking, S., Mahtta, R., Milliman, T., Esch, T., and Seto, K. C.: Global urban structural growth shows a profound shift from spreading out to building up, Nature Cities, 1(9), 555-566, https://doi.org/10.1038/s44284-024-00100-1, 2024

Geiß, C., Schrade, H., Pelizari, P. A., and Taubenböck, H.: Multistrategy ensemble regression for mapping of built-up density and height with Sentinel-2 data, ISPRS journal of photogrammetry and remote sensing, 170, 57-71, https://doi.org/10.1016/j.isprsjprs.2020.10.004, 2020

Gong, P., Li, X., Wang, J., Bai, Y., Chen, B., Hu, T., Liu, X., Xu, B., Yang, J., Zhang, W., and Zhou, Y.: Annual maps of global artificial impervious area (GAIA) between 1985 and 2018, Remote Sensing of Environment, 236, 111510, https://doi.org/10.1016/j.rse.2019.111510, 2020

Gorelick, N., Hancher, M., Dixon, M., Ilyushchenko, S., Thau, D., and Moore, R.: Google Earth Engine: Planetary-scale geospatial analysis for everyone, Remote sensing of Environment, 202, 18-27, https://doi.org/10.1016/j.rse.2017.06.031, 2017

He, T., Wang, K., Xiao, W., Xu, S., Li, M., Yang, R., and Yue, W.: Global 30 meters spatiotemporal 3D urban expansion dataset from 1990 to 2010, Scientific data, 10(1), 321, https://doi.org/10.1038/s41597-023-02240-w, 2023

Hu, T., Zhang, M., Li, X., Wu, T., Ma, Q., Xiao, J., Huang, X., Guo, J., Li, Y., and Liu, D.: Extraction of Building Construction Time Using the LandTrendr Model With Monthly Landsat Time Series Data, IEEE Journal of Selected Topics in Applied Earth Observations and Remote Sensing, 17, 18335-18350, https://doi.org/10.1109/jstars.2024.3409157, 2024

Huang, H., Chen, P., Xu, X., Liu, C., Wang, J., Liu, C., Clinton, N., and Gong, P.: Estimating building height in China from ALOS AW3D30, ISPRS Journal of Photogrammetry and Remote Sensing, 185, 146-157, https://doi.org/10.1016/j.isprsjprs.2022.01.022, 2022

Huang, H., Wang, J., Liu, C., Liang, L., Li, C., and Gong, P.: The migration of training samples towards dynamic global land cover mapping, ISPRS Journal of Photogrammetry and Remote Sensing, 161, 27-36, https://doi.org/10.1016/j.isprsjprs.2020.01.010, 2020

Huang, X., Cao, Y., and Li, J.: An automatic change detection method for monitoring newly constructed building areas using time-series multi-view high-resolution optical satellite images, Remote Sensing of Environment, 244, 111802, https://doi.org/10.1016/j.rse.2020.111802, 2020

Huang, X., and Wang, Y.: Investigating the effects of 3D urban morphology on the surface urban heat island effect in urban functional zones by using high-resolution remote sensing data: A case study of Wuhan, Central China, ISPRS Journal of Photogrammetry and Remote Sensing, 152, 119-131, https://doi.org/10.1016/j.isprsjprs.2019.04.010, 2019

Koppel, K., Zalite, K., Voormansik, K., and Jagdhuber, T.: Sensitivity of Sentinel-1 backscatter to characteristics of buildings, International Journal of Remote Sensing, 38(22), 6298-6318, https://doi.org/10.1080/01431161.2017.1353160, 2017

Li, M., Koks, E., Taubenböck, H., and van Vliet, J.: Continental-scale mapping and analysis of 3D building structure, Remote Sensing of Environment, 245, 111859, https://doi.org/10.1016/j.rse.2020.111859, 2020

Li, S.: Geospatial modelling approach for 3D urban densification developments, ISPRS-international archives of the photogrammetry, remote sensing and spatial information sciences, https://doi.org/10.5194/isprsarchives-xli-b2-349-2016, 2016

Li, X., Zhou, Y., Gong, P., Seto, K. C., and Clinton, N.: Developing a method to estimate building height from Sentinel-1 data, Remote Sensing of Environment, 240, 111705, https://doi.org/10.1016/j.rse.2020.111705, 2020

Liu, M., Ma, J., Zhou, R., Li, C., Li, D., and Hu, Y.: High-resolution mapping of mainland China's urban floor area, Landscape and Urban Planning, 214, 104187, https://doi.org/10.1016/j.landurbplan.2021.104187, 2021

Lyu, R., Zhang, J., Pang, J., and Zhang, J.: Modeling the impacts of 2D/3D urban structure on PM2. 5 at high resolution by combining UAV multispectral/LiDAR measurements and multi-source remote sensing images, Journal of Cleaner Production, 437, 140613, https://doi.org/10.1117/12.2031094, 2024

Ma, X., Zheng, G., Xu, C., Moskal, L. M., Gong, P., Guo, Q., Huang, H., Li, X., Liang, X., Pang, Y., Wang, C., Xie, H., Yu, B., Zhao, B., and Zhou, Y.: A global product of 150-m urban building height based on spaceborne lidar, Scientific Data, 11(1), 1387, https://doi.org/10.1038/s41597-024-04237-5, 2024

Ma, X., Zheng, G., Chi, X., Yang, L., Geng, Q., Li, J., and Qiao, Y.: Mapping fine-scale building heights in urban agglomeration with spaceborne lidar, Remote Sensing of Environment, 285, 113392, https://doi.org/10.1016/j.rse.2022.113392, 2023

Marconcini, M., Metz-Marconcini, A., Esch, T., and Gorelick, N.: Understanding current trends in global urbanisation-the world settlement footprint suite, GI_Forum, 9(1), 33-38, https://doi.org/10.1553/giscience2021_01_s33, 2021

Masek, J. G., Vermote, E. F., Saleous, N. E., Wolfe, R., Hall, F. G., Huemmrich, K. F., Gao, F., Kutler, J., and Lim, T. K.: A Landsat surface reflectance dataset for North America, 1990-2000, IEEE Geoscience and Remote sensing letters, 3(1), 68-72, https://doi.org/10.1109/LGRS.2005.857030, 2006

Peters, R., Dukai, B., Vitalis, S., van Liempt, J., and Stoter, J.: Automated 3D reconstruction of LoD2 and LoD1 models for all 10 million buildings of the Netherlands, Photogrammetric Engineering and Remote Sensing, 88(3), 165-170, https://doi.org/10.14358/pers.21-00032r2, 2022

Qi, F., Zhai, J. Z., and Dang, G.: Building height estimation using Google Earth, Energy and Buildings, 118, 123-132, https://doi.org/10.1016/j.enbuild.2016.02.044, 2016

https://doi.org/10.5194/essd-2025-632
Preprint. Discussion started: 9 December 2025

Resch, E., Bohne, R. A., Kvamsdal, T., and Lohne, J.: Impact of urban density and building height on energy use in cities, Energy Procedia, 96, 800-814, https://doi.org/10.1016/j.egypro.2016.09.142, 2016

Schug, F., Frantz, D., van der Linden, S., and Hostert, P.: Gridded population mapping for Germany based on building density, height and type from Earth Observation data using census disaggregation and bottom-up estimates, Plos one, 16(3), e0249044, https://doi.org/10.1371/journal.pone.0249044, 2021

Stanimirova, R., Tarrio, K., Turlej, K., McAvoy, K., Stonebrook, S., Hu, K. T., Arévalo, P., Bullock, E. L., Zhang, Y., Woodcock, C. E., Olofsson, P., Zhu, Z., Barber, C. P., Souza Jr, C. M., Chen, S., Wang, J. A., Mensah, F., Calderón-Loor, M., Hadjikakou, M., Bryan, B. A., Graesser, J., Beyene, D. L., Mutasha, B., Siame, S., Siampale, A., and Friedl, M. A.: A global land cover training dataset from 1984 to 2020, Scientific Data, 10(1), 879, https://doi.org/10.1038/s41597-023-02798-5, 2023

Stilla, U., and Xu, Y.: Change detection of urban objects using 3D point clouds: A review, ISPRS Journal of Photogrammetry and Remote Sensing, 197, 228-255, https://doi.org/10.1016/j.isprsjprs.2023.01.010, 2023

Stipek, C., Hauser, T., Adams, D., Epting, J., Brelsford, C., Moehl, J., Dias, P., Piburn, J., and Stewart, R.: Inferring building height from footprint morphology data, Scientific Reports, 14(1), 18651, https://doi.org/10.1038/s41598-024-66467-2, 2024

Sun, X., Huang, X., Mao, Y., Sheng, T., Li, J., Wang, Z., Lu, X., Ma, X., Tang, D., and Chen, K.: GABLE: A first fine-grained 3D building model of China on a national scale from very high resolution satellite imagery, Remote Sensing of Environment, 305, 114057, https://doi.org/10.1016/j.rse.2024.114057, 2024

Vermote, E., Justice, C., Claverie, M., and Franch, B.: Preliminary analysis of the performance of the Landsat 8/OLI land surface reflectance product, Remote sensing of environment, 185, 46-56, https://doi.org/10.1016/j.rse.2016.04.008, 2016

Wang, Y., Li, X., Yin, P., Yu, G., Cao, W., Liu, J., Pei, L., Hu, T., Zhou, Y., Liu, X., Huang, J., and Gong, P.: Characterizing annual dynamics of urban form at the horizontal and vertical dimensions using long-term Landsat time series data, ISPRS Journal of Photogrammetry and Remote Sensing, 203, 199-210, https://doi.org/10.1016/j.isprsjprs.2023.07.025, 2023

Wu, F.: State dominance in urban redevelopment: Beyond gentrification in urban China, Urban Affairs Review, 52(5), 631-658, https://doi.org/10.1177/1078087415612930, 2016

Wu, W. B., Ma, J., Banzhaf, E., Meadows, M. E., Yu, Z. W., Guo, F. X., Sengupta, D., Cai, X. X., and Zhao, B.: A first Chinese building height estimate at 10 m resolution (CNBH-10 m) using multi-source earth observations and machine learning, Remote Sensing of Environment, 291, 113578, https://doi.org/10.1016/j.rse.2023.113578, 2023

Yadav, R., Nascetti, A., and Ban, Y.: How high are we? Large-scale building height estimation at 10 m using Sentinel-1 SAR and Sentinel-2 MSI time series, Remote Sensing of Environment, 318, 114556, https://doi.org/10.2139/ssrn.4762421, 2025

Yan, W., Wu, J., Zhang, C., Chen, X., Ren, J., Xiao, Z., Liao, Z., Lafortezza, R., and Su, Y.: Developing an annual building volume dataset at 1-km resolution from 2001 to 2019 in China, International Journal of Digital Earth, 17(1), 2330690, https://doi.org/10.1080/17538947.2024.2330690, 2024

Yang, J., Yang, Y., Sun, D., Jin, C., and Xiao, X.: Influence of urban morphological characteristics on thermal environment, Sustainable Cities and Society, 72, 103045, https://doi.org/10.1016/j.scs.2021.103045, 2021

https://doi.org/10.5194/essd-2025-632
Preprint. Discussion started: 9 December 2025

Yuan, B., Yu, G., Li, X., Li, L., Liu, D., Guo, J., and Li, Y.: Reconstructing Long-Term Synthetic Aperture Radar Backscatter in Urban Domains Using Landsat Time Series Data: A Case Study of Jing–Jin–Ji Region, Journal of Remote Sensing, 4, 0172, https://doi.org/10.34133/remotesensing.0172, 2024

Zhang, L., and Weng, Q.: Annual dynamics of impervious surface in the Pearl River Delta, China, from 1988 to 2013, using time series Landsat imagery, ISPRS Journal of Photogrammetry and Remote Sensing, 113, 86-96, https://doi.org/10.1016/j.isprsjprs.2016.01.003, 2016

Zhang, Y., Wang, Y., Dong, Q., Chen, X., Zhang, F., Li, X. and Liu, Y.: Mapping Three Decades of Urban Growth in China: A 30m Annual Building Height Dataset (1990 – 2019) [data set], https://doi.org/10.6084/m9.figshare.29918978, 2025

Zhang, Y., Zhao, H., and Long, Y.: CMAB: A Multi-Attribute Building Dataset of China, Scientific Data, 12(1), 430, https://doi.org/10.1038/s41597-025-04730-5, 2025

Zhao, X., Xia, N., and Li, M.: Dynamic monitoring of urban renewal based on multi-source remote sensing and POI data: A case study of Shenzhen from 2012 to 2020, International Journal of Applied Earth Observation and Geoinformation, 125, 103586, https://doi.org/10.1016/j.jag.2023.103586, 2023

Zhou, Y., Li, X., Chen, W., Meng, L., Wu, Q., Gong, P., and Seto, K. C.: Satellite mapping of urban built-up heights reveals extreme infrastructure gaps and inequalities in the Global South, Proceedings of the National Academy of Sciences, 119(46), e2214813119, https://doi.org/10.1073/pnas.2214813119, 2022

Zhu, X. X., Chen, S., Zhang, F., Shi, Y., and Wang, Y.: GlobalBuildingAtlas: An open global and complete dataset of building polygons, heights and LoD1 3D models. arXiv preprint arXiv:2506.04106.

Zhu, Z., and Woodcock, C. E.: Continuous change detection and classification of land cover using all available Landsat data, Remote sensing of Environment, 144, 152-171, https://doi.org/10.1016/j.rse.2014.01.011, 2014